Journal of Volcanology and Geothermal Research 443 (2023) 107914

Contents lists available at ScienceDirect

Journal of Volcanology and Geothermal Research

journal homepage: www.journals.elsevier.com/journal-of-volcanology-and-geothermal-research

Feeders vs arrested dikes: A case study from the Younger Stampar eruption in Iceland

Noemi Corti [a], Fabio L. Bonali [a,b,*], Elena Russo [a,b], Kyriaki Drymoni [a], Federico Pasquaré Mariotto [c], Agust Gudmundsson [d], Rosario Esposito [a], Alessandro Cavallo [a], Alessandro Tibaldi [a,b]

[a] Department of Earth and Environmental Sciences, University of Milan-Bicocca, 20126 Milan, Italy
[b] CRUST-Interuniversity Centre for 3D Seismotectonics with Territorial Applications, 66100 Chieti Scalo, Italy
[c] Department of Human and Innovation Sciences, Insubria University, Como, Italy
[d] Department of Earth Sciences, Queen's Building, Royal Holloway University of London, Egham TW20 0EX, UK

ARTICLE INFO

Keywords:
Younger Stampar eruption
Reykjanes Peninsula
Dike
Crustal deformation
Numerical modelling

ABSTRACT

Understanding the mechanical conditions for dike arrest and associated surface deformation or, alternatively, dike propagation to the surface to supply magma to an eruption, is of fundamental importance for volcanology in general and for volcanic hazards in particular. Here we present the results of a study of an outcrop located in the Reykjanes Peninsula, SW Iceland, where one dike became arrested only 5 m below the surface of an active volcanic system, without inducing any brittle deformation at the surface. In the same outcrop, at a distance of 30 m, a feeder dike is exposed. Both dikes are associated with the Younger Stampar eruption (1210–1240 CE). We reconstructed a high-resolution 3D model, through drone surveys and Structure from Motion (SfM) techniques, on which we collected detailed structural data combined with field surveys. These data, integrated with petrographic and geochemical analyses, became inputs to Finite Element Method (FEM) numerical models, made using the COMSOL Multiphysics® software. Our results indicate that compression exerted by the intrusion of the feeder dike (inferred to have been emplaced first) can explain the arrest of the second dike and the absence of induced brittle deformation even if the dike tip is only 5 m below the surface. Furthermore, the contrasting mechanical properties of the layers that constitute the outcrop, with alternating stiff lavas and compliant tuffs, raise (concentrate) the compressive stresses in the lava flows ahead of the second dike, thereby encouraging its arrest. Both the dikes are basaltic, but the earlier emplaced feeder dike is crystal poor and slightly more evolved than the later emplaced arrested dike. The results throw a new light on the conditions for dike arrest and (the lack of) dike-induced brittle deformation at very shallow depths in active rift zones, with important implications for volcanic-hazard assessments.

1. Introduction

During volcanic eruptions, magma is transported up to the surface through magma-filled fractures, dikes or inclined sheets, driven mainly by internal magmatic overpressure (Delaney et al., 1986; Gudmundsson, 2011a, 2020; Acocella, 2021). However, observations show that most dikes do not reach the surface to supply magma to eruptions (Gudmundsson et al., 1999; Gudmundsson and Brenner, 2001; Gudmundsson, 2003; Calais et al., 2008; Pallister et al., 2010; Bonaccorso et al., 2011; Nobile et al., 2012; Rivalta et al., 2015; Townsend et al., 2017). Most of the dikes that do not reach the surface become arrested at contacts between mechanically dissimilar layers or, alternatively, become deflected into sills (Gudmundsson, 1986a; Parsons et al., 1992; Kavanagh et al., 2006; Rivalta et al., 2005; Thomson, 2007; Menand, 2008; Tibaldi and Pasquarè Mariotto, 2008; Gudmundsson, 2011a, 2011b; Maccaferri et al., 2011; Drymoni et al., 2020). On approaching the surface, dikes generate stress in the host rock (Rubin and Gillard, 1998; Gudmundsson, 2003, 2011a; Roman and Cashman, 2006; Ágústsdóttir et al., 2016; Bazargan and Gudmundsson, 2019, 2020; Heimisson and Segall, 2020), which can lead to surface deformation, normal faults, graben structures, or dry tension fractures (Swanson, 1976; Pollard et al., 1983; Murray and Pullen, 1984; Mastin and Pollard,

* Corresponding author at: Department of Earth and Environmental Sciences, University of Milan-Bicocca, 20126 Milan, Italy.
E-mail address: fabio.bonali@unimib.it (F.L. Bonali).

https://doi.org/10.1016/j.jvolgeores.2023.107914
Received 8 June 2023; Received in revised form 11 September 2023; Accepted 17 September 2023
Available online 22 September 2023
0377-0273/© 2023 The Author(s). Published by Elsevier B.V. This is an open access article under the CC BY-NC-ND license (http://creativecommons.org/licenses/by-nc-nd/4.0/).

1988; Rubin and Pollard, 1988; Gudmundsson, 2003; Nobile et al., 2012; Segall, 2013; Trippanera et al., 2015; Magee and Jackson, 2021; Tibaldi et al., 2022). Dike-induced grabens have been observed along both fast and slow-spreading plate boundaries (Stein et al., 1991; Chadwick Jr and Embley, 1998; Wright et al., 2006; Calais et al., 2008; Ebinger et al., 2008; Biggs et al., 2009; Grandin et al., 2009; Pallister et al., 2010; Acocella and Trippanera, 2016; Xu et al., 2016; Al Shehri and Gudmundsson, 2018; Trippanera et al., 2019; Gudmundsson, 2020; Tibaldi et al., 2022), including in Iceland, during the recent Krafla and Bardarbunga rifting episodes (Sigurdsson, 1980; Rubin, 1992; Sigmundsson et al., 2015; Hjartardóttir et al., 2016; Ruch et al., 2016). Over the past decades, the studies on the relations between dike intrusions and surface deformation have become key to volcanic hazard assessment, through analytical (Isida, 1955), analogue (Mastin and Pollard, 1988; Trippanera et al., 2015; Xu et al., 2016) and numerical studies (Pollard et al., 1983; Rubin and Pollard, 1988; Bazargan and Gudmundsson, 2019, 2020; Clunes et al., 2023). However, detailed field studies of dikes and faults in Iceland show no connection between grabens (or normal faults in general) and dikes (Forslund and Gudmundsson, 1991, 1992), and there is evidence of arrested dikes in different volcanic areas that are not associated with fracturing and/or faulting around the dike tip or at the surface (e.g., Gudmundsson, 2003). These observations and related numerical models suggest that no dike-induced surface deformation would normally be expected, unless the tip of the dike is at a depth < 1 km (Al Shehri and Gudmundsson, 2018).

Here, we present a case study of two dikes. One became arrested at a depth of only 5 m below the surface of an active rift zone without inducing deformation at the surface. Only 30 m away is an outcrop of a feeder dike (Sigurgeirsson, 1995; Gudmundsson, 2017), referred to as the first dike (it is inferred to have been emplaced earlier than the arrested (second) dike). Both dikes belong to the Younger Stampar magmatic system that produced eruptions in 1210–1240 CE (Saemundsson et al., 2016) on the Reykjanes Peninsula (RP), SW Iceland (Fig. 1). We collected new quantitative data from a high-resolution 3D model, using photogrammetry techniques, made field surveys, and performed petrographic and geochemical analyses on both dikes. Subsequently, we made a set of Finite Element Method (FEM) numerical models using the COMSOL Multiphysics® software to explore possible scenarios regarding the conditions for dike arrest and lack of surface deformation.

The aim of this paper is to address the following research issues: *(i)* What factors contributed to the arrest of the second dike? *(ii)* Why is there no deformation at the surface associated with the arrested dike? *(iii)* What are the petrographic and geochemical differences between the first (feeder) and second (arrested) dike and what is their relation to the other historical lava flow on the RP?

Our study focuses on dike emplacement and arrest and is highly relevant to dike propagation and eruptions, as occurred in Fagradalsfjall on the RP in 2021–2022. Considering the cyclic nature of eruptive activity in the RP (Saemundsson et al., 2020), the results of our study should improve the understanding of present-day and future eruptions on the RP, with implications for other similar volcanic areas around the world.

2. Geological setting

The Reykjanes Peninsula (RP) extends with an overall trend of N70°E, strongly oblique to the spreading direction of N101°E (DeMets et al., 2010, Fig. 1). This leads to the coexistence of volcanism and intense seismicity in the RP differently from other volcanic systems in Iceland, which are mostly characterised by weaker seismicity (Einarsson, 2008). From west to east, four volcanic systems, which also contain fissure swarms, have been identified, namely those of Reykjanes, Krísuvík, Brennisteinsfjöll and Hengill (Einarsson and Saemundsson, 1987), each consisting of eruptive fissures, normal faults and tension fractures (Fig. 1). On the RP, rifting episodes occur every 800–1000 years affecting different volcanic systems. Starting from 14,500 yr BP, volcanic fissures became dominant in the RP (Saemundsson et al., 2020). The volcanic systems have a general northeast strike (Clifton and Schlische, 2003) and the eruptive fissures are marked by alignments of scoria and spatter cones. Before the 2021–2022 volcanic activity, the latest volcanic episode on the RP took place between 700 and 1240 CE inducing

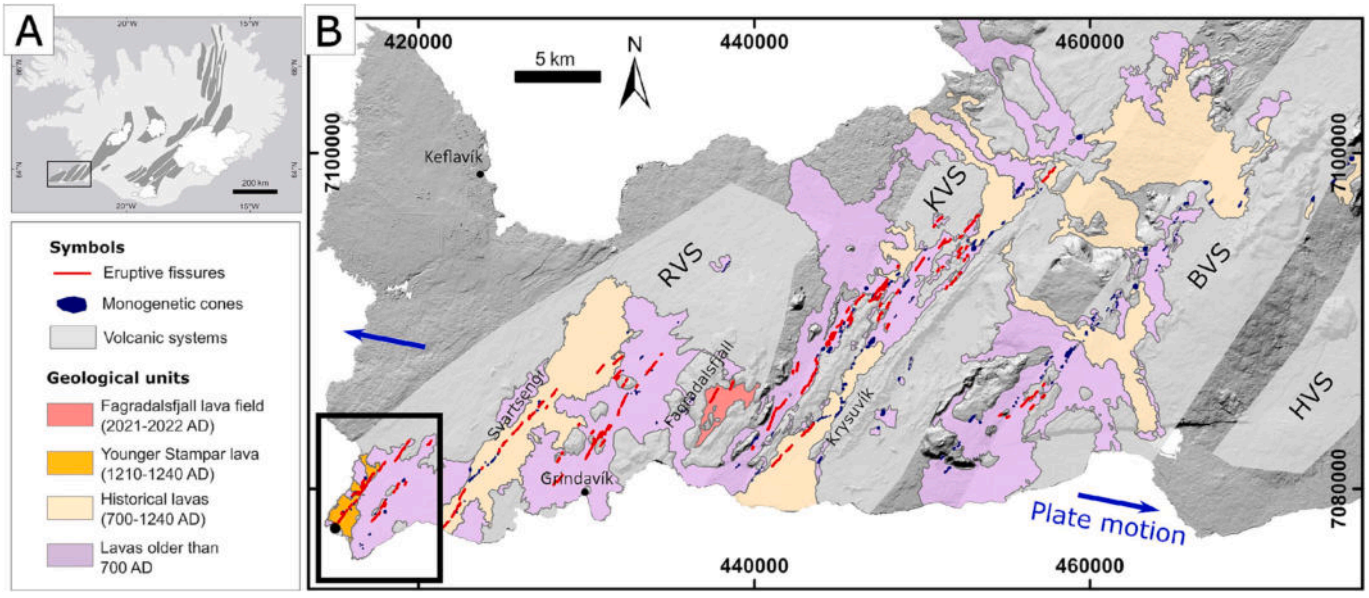

Fig. 1. (A) Main volcanic zones of Iceland (from Einarsson, 2008), spatial reference: WGS84 - Geographic coordinates. (B) Map showing the volcanic systems in the RP (after Einarsson and Saemundsson, 1987), and historical and prehistoric lava fields (from Saemundsson et al., 2016), including the Younger Stampar and the 2021–2022 Fagradalsfjall lava flows (from https://geovis.hi.is/). Eruptive fissures and monogenetic cones are shown in red and blue, respectively (from Saemundsson et al., 2016). Spatial reference: WGS 84 - UTM zone 27 N. RVS: Reykjanes Volcanic System, KVS: Krísuvík Volcanic System, BVS: Brennisteinsfjöll Volcanic System, HVS: Hengill Volcanic System. Blue arrows show the plate motion direction, the spreading vector (N101°E, from DeMets et al., 2010). The DEM in the background is the 2-m resolution Arctic DEM (https://www.pgc.umn.edu/data/arcticdem/). The black box indicates the location of the study area. The black dot inside the box locates the studied outcrop. (For interpretation of the references to colour in this figure legend, the reader is referred to the web version of this article.)

fissure eruptions with the same NE orientation (Saemundsson et al., 2016, 2020) (Fig. 1).

The Reykjanes Volcanic System, which includes the Reykjanes Fissure Swarm (RFS), is the westernmost one in the RP, with a total length of 45 km, 30 km of which are located on land. Fissure eruptions in the RFS are marked by onshore effusive activity and offshore hydrovolcanic activity, based on the latest volcanic activity (early 13th Century), which included the Younger Stampar eruption (Sigurgeirsson, 1995). This is the youngest of the three volcanic events, denominated "Stampar" eruptions. The oldest lava flow is dated to 3500–4000 yr BP (Sigurgeirsson, 1992) while the youngest two lava flows are called "Older Stampar" and "Younger Stampar" and are dated to 2000 yr BP and the 13th Century, respectively (Figs. 2A). These latter two lava flows erupted on land along 7-km long and 4-km long crater rows, respectively (Fig. 2A-B).

We concentrate on the most recent event, the Younger Stampar eruption. This was part of the Reykjanes Fires, an eruptive episode that occurred between 1210 and 1240 CE (Saemundsson et al., 2016). The earlier phase of the event occurred offshore, characterised by Surtseyan eruptions that resulted in the formation of two tuff cones. The youngest cone, called Karl, has been mostly eroded by the sea, leaving a 50-m high pillar (Fig. 2A). After this offshore phase, a 4-km-long volcanic fissure opened on land, triggering a Hawaiian eruption (Sigurgeirsson, 1995).

Along the sea-cliff to the SW, there are the two studied dikes related to this magmatic system (Sigurgeirsson, 1995; Gudmundsson, 2017) (Fig. 2C and Fig. 3). The arrested dike cuts through a soft tuff layer, made of tephra deposits from the Karl crater, dated to 1211 CE using tephrochronology, ^{14}C dating, and written sources (Sigurgeirsson, 1995; Saemundsson et al., 2020), but becomes arrested when it reaches the contact between the tuff and the Younger Stampar lava flow (Gudmundsson, 2017). The feeder dike is located some 30 m to the northeast of the arrested dike and fed only the upper part of the flow, but not its lower part, which had erupted before from the Karl cone (Sigurgeirsson, 1995; Gudmundsson, 2017).

3. Methodology

To perform a complete analysis of the study area, we used a multidisciplinary approach, illustrated in the workflow in Fig. 4. Firstly, we collected structural data and representative samples for petrographic and geochemical analyses. Specifically, we obtained a high-resolution structural geological dataset using mainly 3D models and field campaigns. Then we combined literature data and petrographic and geochemical analyses to obtain the composition of the dikes. Finally, our data became inputs to FEM numerical models that allowed us to investigate the parameters that control dike propagation and surface deformation in the shallow crust. We would like to highlight that the thickness of the volcanic layers and dikes had been measured previously during field surveys (Gudmundsson, 2017). In this work, we collected new measurements through drone surveys and SfM-derived 3D models that allowed us to collect more accurate data, reaching also the highest part of the cliff. Furthermore, due to its location, the outcrop is strongly

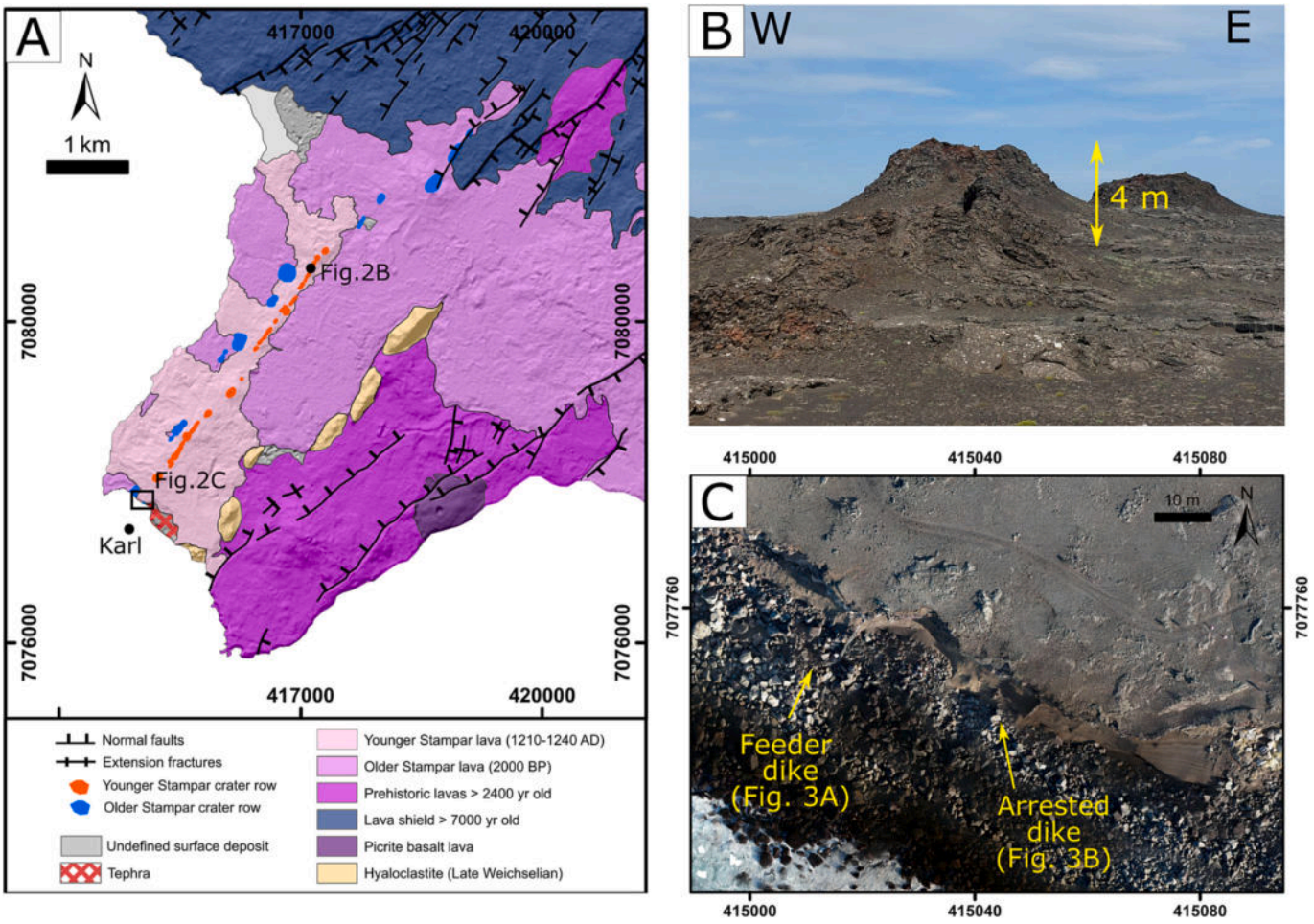

Fig. 2. A) Geological-structural map of the area showing the Older and Younger Stampar eruptions, modified after Saemundsson et al. (2016) with the help of aerial photographs. The crater rows associated with these eruptions and the location of the Karl cone are highlighted. Spatial reference: WGS 84 - UTM zone 27 N. B) Aligned scoria and spatter cones of the Younger Stampar crater row (location in Fig. 2A). C) Plan view of the dikes cropping out along the edge of the cliff, observed on a high-resolution orthomosaic (location in Fig. 2A). Spatial reference: WGS 84 - UTM zone 27 N.

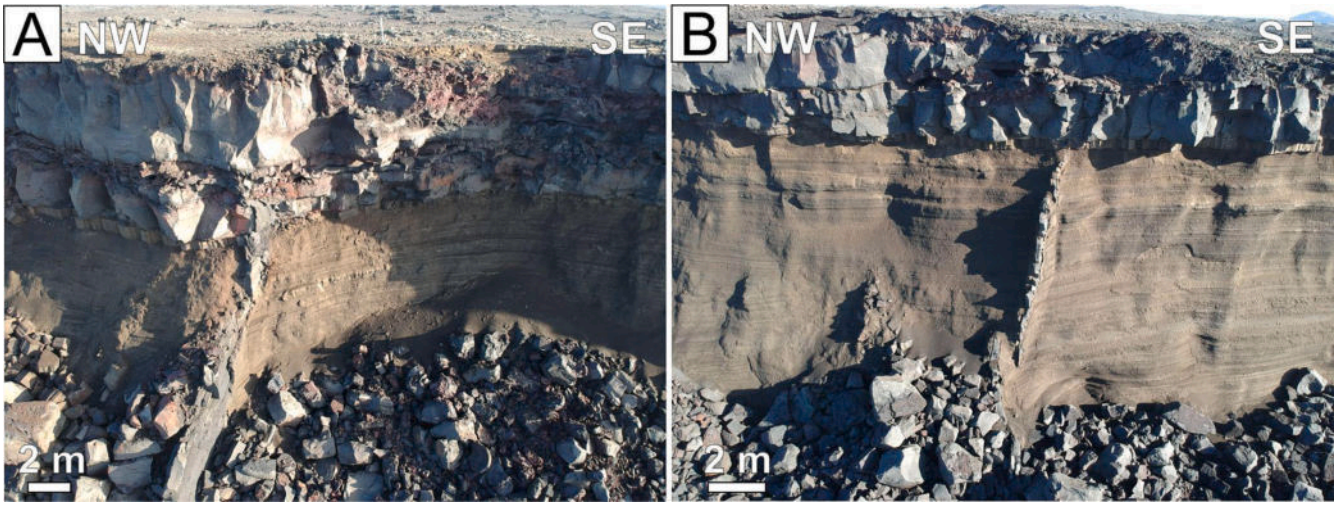

Fig. 3. UAV-captured pictures showing A) the feeder dike (occasionally referred to as the first dike) and B) the arrested dike (occasionally referred to as the second dike). The locations of the two dikes are shown in Fig. 2C.

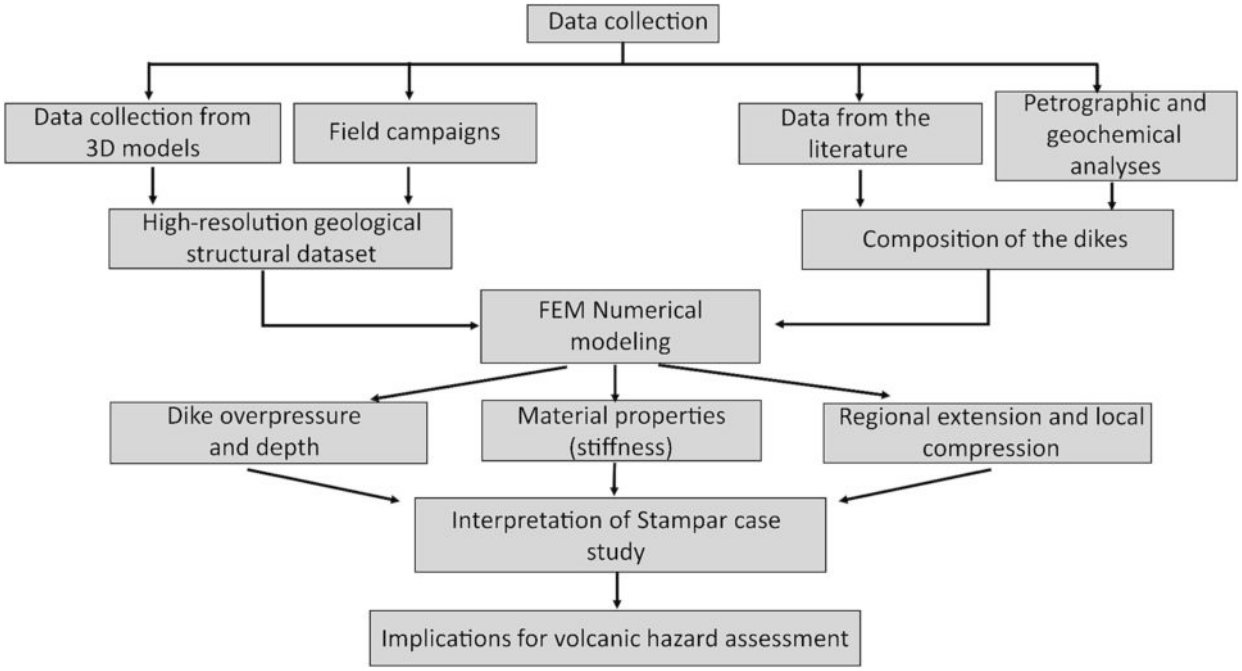

Fig. 4. Multidisciplinary workflow representing the steps followed in the present study.

affected by marine erosion, meaning that the parts of the dikes that are available for measurements in the cliffs (Fig. 3) change as erosion progresses. This can explain the difference between our measurements and the previous ones. The methodology steps are presented in the following sections.

3.1. Structural data collection through field surveys and on photogrammetry-derived 3D models

To map the study area, we used aerial photographs collected in 1981, 1984 and 1988, available from the National Land Survey of Iceland website (https://www.lmi.is/). We carried out the photogrammetric processing of these images (e.g., Micheletti et al., 2015; Bonali et al., 2019) through the SfM software Agisoft Metashape (https://www.agisoft.com/), to obtain orthomosaics and Digital Surface Models (DSMs) with resolutions up to 20 and 40 cm/pixel, respectively. Using the resulting models and the geological map of SW Iceland at the scale of 1:100,000 (Saemundsson et al., 2016), we mapped all the lava flows, geological units and the main structures of the area, as well as the volcanic fissures of the Stampar craters (Fig. 2A). We distinguished normal faults from tension fractures based on the presence of shaded or brighter-lit slopes, highlighting the presence of a fault scarp (e.g., Corti et al., 2021). We mapped the base of each vent along the crater rows, and traced the eruptive fissures based on the elongation of each spatter cone, which is considered parallel to the strike of the underlying dike (Tibaldi, 1995; Tibaldi and Bonali, 2017). All the mapped structures were validated during field surveys conducted during the summer seasons of 2021 and 2022.

To collect structural data from the dikes and the studied outcrops, we built a high-resolution 3D model derived from 1073 Unmanned Aerial Vehicle (UAV)-collected pictures. We used a DJI Spark, a small quadcopter equipped with a 12 Megapixels camera, which had been

successfully employed before in other volcanic areas (Bonali et al., 2020). The camera was set orthogonal to the cliff (oblique orientation) for 360 pictures, whereas a classical nadir orientation was used for the others. The drone was manually flown at a speed of 2 m/s and images were captured every 2 s, flying at a distance of about 20–25 m from the target, similarly to the method of Pasquaré Mariotto et al. (2021). We performed the photogrammetric processing (James and Robson, 2012; Burns and Delparte, 2017; James et al., 2017) with high quality settings, obtaining a 3D model with texture resolution of 0.8 cm/pixel, together with an orthomosaic (0.8 cm/pixel) (Fig. 2C) and a DSM (1 cm/pixel). We georeferenced and scaled the model placing 6 Ground Control Points (GCPs) collected using single frequency receivers in real-time kinematic (RTK) positioning configuration (2 cm of accuracy). We also carried out quantitative data collection on the resulting models in Agisoft Metashape and GIS environments, measuring the thickness of the volcanic layers and the attitude and thickness of the two dikes.

3.2. Petrography and geochemistry of the dikes

Here we report preliminary petrographical and geochemical results based on four representative samples, two from the feeder and two from the arrested dike. We collected the samples at the contact between the dike and the host rock wall, and they all include a glassy margin <0.5 cm. Both dikes were sampled at a height of about 5.5 m a.s.l., and at a similar distance from the host rock contact, at least at 1–1.5 cm from the chilled margin. We pulverised and pressed them as pellets for the analysis. We performed whole rock analyses using the energy-dispersive X-ray fluorescence (EDXRF) furnished with a PANalytical Epsilon 3-XL spectrometer at the University of Milan-Bicocca, similarly to that done by Tibaldi et al. (2013). We analysed the dikes for major and minor elements (Si, Ti, Al, Fe, Mn, Mg, Ca, Na, K and P) based on EDXRF and through the Malvern Panalytical Epsilon 3 software platform, using calibration curves based on basaltic international standards. Relative errors are <6% for all the elements with the exception of K_2O (13%) and P_2O_5 (21%) which are showing concentration always <0.2 wt%.

Two thin sections (30 μm) for each dike were prepared. We obtained the modal composition using an optical microscope and the JMacroVision software based on random point analysis with a total of 2000 points for each thin section. We used a Secondary Electron Microscope (Vega TS Tescan 5163 XM) combined with an Energy Dispersive X-ray Spectrometer analyser (EDAX Genesis 400) at the University of Milan-Bicocca to analyse plagioclase, clinopyroxene and olivine phenocrysts (>5 mm) and microphenocrysts for major elements, using the same method as Borromeo et al. (2022). We analysed the phenocrysts both in the core and in the rim to test for chemical zoning, using 20 kV for the accelerating voltage, and 200 pA for the beam current. We applied corrections for the atomic number, absorption and fluorescence excitation effects (ZAF correction) for the mineral analyses. For plagioclase concentrations, the relative errors of SiO_2, Al_2O_3, CaO, and Na_2O are <1%, for K_2O is 13%. For clinopyroxene concentrations, the relative errors of SiO_2, MgO, and CaO are <1%, for FeO and Al_2O_3 are 7% and 9% respectively, and for Cr_2O_3 and Na_2O are 15%. Finally, for olivine, the relative errors of major element concentrations are <1% for SiO_2 and MgO, and 2% for FeO.

3.3. Numerical modelling setup

We made numerical models using COMSOL Multiphysics (v5.6), a FEM software which can be used to study the distribution of dike-induced local stresses, displacements, and strains subject to user-defined boundary loads. We designed a 500 × 500 m squared domain and discretised it by a very fine triangular meshing, with a minimum element quality of 0.4534 m and 1100 boundary triangular elements. We inserted the dike as a fluid-filled cavity and arranged it in the central part of the domain to exclude edge effects from our interpretations (Drymoni et al., 2023). We fastened the models in the two bottom corners to avoid rigid-body rotation and translation (Geyer and Gottsmann, 2010; Browning et al., 2021). We developed static models by placing the dike along the vertical (Y) axis arbitrarily to simulate vertical dike propagation (Fig. 5A).

We used previous field observations and our 3D structural data to replicate an elastic layered medium (Sigurgeirsson, 1995; Gudmundsson, 2017). We assigned distinct mechanical properties (e.g., Young's modulus (E), density (ρ), Poisson's ratio (ν)) for each layer based on typical values from the literature (Gudmundsson, 2011a, 2020). From top to bottom, the stratigraphic column is composed as follows:

- Upper lava unit, 2 m thick, $E_{UL} = 10$ GPa, $\rho = 2600$ kg/m^3, $\nu = 0.25$;
- Lower lava unit, 2.6 m thick, $E_{LL} = 11$ GPa, $\rho = 2600$ kg/m^3, $\nu = 0.25$;
- Consolidated ash, 0.4 m thick, $E_A = 5$ GPa, $\rho = 2300$ kg/m^3, $\nu = 0.25$;
- Tuff, 10 m thick, $E_T = 1$ GPa, $\rho = 2000$ kg/m^3, $\nu = 0.25$;
- Pillow lavas, $E_{PL} = 10$ GPa, $\rho = 2700$ kg/m^3, $\nu = 0.25$. This layer is not present in the outcrop. However, we included it in the stratigraphy based on the offshore available data.

We applied different boundary conditions, such as: *a)* a range of overpressure ($P_o = 2$–4 MPa), based on previous studies (Gudmundsson, 2011a, 2020; Drymoni et al., 2020), *b)* an 1 MPa horizontal extensional stress (Fig. 5A-B) to simulate plate motion (Fig. 1), and *c)* a horizontal compressional stress (1–4 MPa), applied to all the layers cut by the feeder dike, simulating the effect of compression in the host rock caused by the magmatic overpressure of the previous dike intrusion (Gudmundsson, 2017) (Fig. 5C).

We plotted the stress values at the tip of the dike and at its vicinity, namely the maximum principal tensile stress (σ_3) and the absolute shear stress (τ). We produced 1D graphs of tensile and von Mises shear stresses (τ) at the surface, to investigate the likelihood of tensile fracture formation or the possibility of fault initiation or, possibly, a slip on a pre-existing fracture. For a tension fracture to form, the tensile stress (σ_3) should be at least equal to the in-situ tensile strength (T_0) of the host rock (0.5–9 MPa, Amadei and Stephansson, 1997), with the most typical values between 2 and 4 MPa (Gudmundsson, 2011a). For fault formation, the von Mises shear stress (τ) must be two times the tensile stress ($\tau \geq 2\sigma_3$), namely 4–8 MPa (Haimson and Rummel, 1982; Schultz, 1995). Furthermore, we studied the trajectories (ticks) of the maximum (σ_1) and minimum (σ_3) principal compressive stresses (σ_3 is also the maximum principal tensile stress), to investigate the dike arrest or propagation path.

We divided our numerical models in three settings:

- Setting I: Investigating the vertical dike propagation in the tuff layer. We moved the arrested dike along the Y axis within the tuff (Y_1, Y_2, Y_3) by applying different overpressure values and an extensional stress field of 1 MPa (Fig. 5A);
- Setting II: Exploring the mechanical properties for the tuff and lava layers and their effect on dike propagation. We gave a range of different Young's modulus ($E_T = 1$–3 GPa) to the tuff layer and the lava layers (E_{UL} and $E_{LL} = 7$–15 GPa). The arrested dike has an overpressure of 3 MPa, and is subject to an extensional tectonic stress field of 1 MPa (Fig. 5B);
- Setting III: Evaluating the influence of compression caused by the pre-existing feeder dike (Gudmundsson, 2017). The Stampar dikes have a similar strike so that we may assume that the horizontal compressive stress induced by the feeder was essentially in a direction perpendicular to the plane of the non-feeder, even if primarily mode I cracks (such as dikes are) can usually deviate slightly from the direction that is exactly perpendicular to σ_3. This could happen particularly if magma finds weaknesses (e.g. joints) with zero tensile strength that are not perfectly perpendicular to the σ_3. Such a deviation is partly a consequence of the dikes following the path of least action (Gudmundsson, 2022). Here, we assigned to the arrested dike overpressure (2 to 4 MPa) and a compressional stress field of 1 to 4 MPa (Fig. 5C).

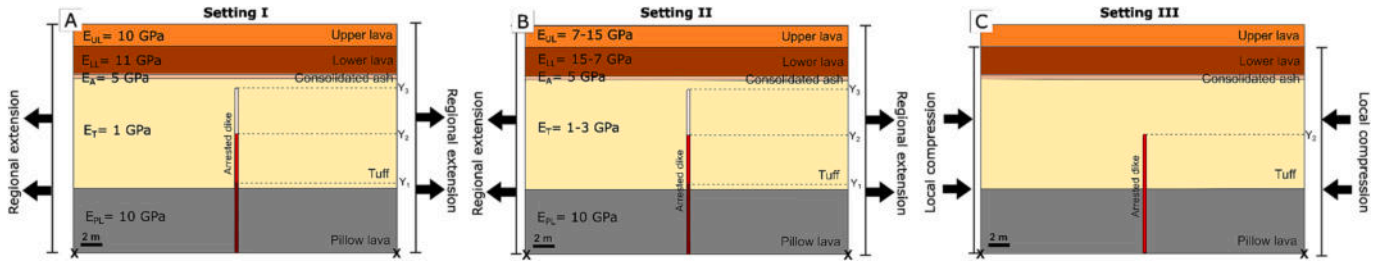

Fig. 5. Numerical models setup. (A) Setting I: investigating dike propagation in the tuff layer subject to dike overpressure and regional extension, represented by black arrows (applied at the boundaries indicated by the black lines on the sides). The arrested dike is represented by dark red, light red, and pink vertical line according to its Y position (Y_1, Y_2, Y_3). (B) Setting II: exploring the influence of mechanical parameters (E) on dike propagation. (C) Setting III: evaluating the effect of the local feeder dike-induced compressional stress field, represented by black arrows (applied at the boundaries indicated by the black lines on the sides). The arrested dike is kept at the constant depth Y_2. In all models, the stratigraphy is based upon field observations. X symbols at the bottom corners represent fixed model constraints. (For interpretation of the references to colour in this figure legend, the reader is referred to the web version of this article.)

4. Results

4.1. Geological and structural data

We identified all the vents (spatter cones) belonging to the Older and the Younger Stampar crater rows, mapping their bases through historical aerial photographs and field surveys (Fig. 6A). Based on the elongation of these cones, we traced 23 eruptive fissures for the Older Stampar, and 49 for the Younger Stampar crater row. We distinguished the two crater rows with the help of previous maps (Sigurgeirsson, 1995) and through field observations. Differences between the two crater rows were visible in the field as the cones that belonged to the Older Stampar fissure were more covered by vegetation than the Younger Stampar ones.

Both crater rows present a general NE-trending alignment (Figs. 6A-B). Based on the eruptive fissures that we traced, the strike for the Older Stampar is between N21°E and N51°E, with an average value of N33.2°E and a standard deviation (SD) of 6.5°, consistent with the alignment orientation (Fig. 6C). The eruptive fissures of the Younger Stampar show a similar range of values, between N23°E to N50°E, with an average value of N38.8°E and a SD of 5.7° (Fig. 6D). No fractures (apart from the eruptive fissure itself) were found in the Younger Stampar area based on our field studies and aerial photographs, as is confirmed by the 3D model in Fig. 6B.

On the high-resolution 3D model reconstructed from drone-collected pictures, we analysed the stratigraphy of the cliff where the two dikes are exposed and measured the thickness of each layer (Fig. 6G). Starting from the bottom, we observed the following units: i) a tuff layer, with a maximum exposed thickness of 10 m; the lowest part of this layer is covered by fallen blocks, so the actual thickness could be greater than the measured value; ii) a thin layer made of consolidated (baked) ash, with a thickness of 0.4 m; iii) a 2.6-m-thick, lower lava layer; iv) an upper lava flow, with thickness decreasing toward the southeast but as much as 2 m above the arrested dike. Above the tip of the feeder dike, it is possible to observe the lava flow fed by the dike itself, which becomes thinner away from the dike (Fig. 6G).

The feeder dike cuts the tuff, the thin baked (heat metamorphosed) and consolidated ash layer, and the lower part of the lava flow, before feeding the lava flow above. The other dike becomes arrested at the contact between the tuff and the baked (consolidated) ash layer (Fig. 6G). We measured the strike of these dikes as follows: 1) the feeder dike shows values between N27°E and N47°E, with an average of N36.2°E and a SD of 7.5° (Fig. 6F); 2) the arrested dike shows values between N18°E and N47°E, with an average of N32.2°E and a SD of 12.6° (Fig. 6E). In general, both dikes present strike values that are consistent with the orientations measured for the crater rows.

The feeder dike has a maximum thickness of 57 cm at the base of the outcrop, which decreases where it cuts the lava, with an average thickness of 30 cm. The dike is everywhere vertical or subvertical, dipping to the NW, with a small deflection to 83° where it enters the lava flow. The exposed part of the arrested dike is made of two segments. The upper segment has maximum and average thicknesses of 16 cm and 10 cm, respectively. The dike propagated vertically, decreasing to 70° to the NW just before it became arrested at the contact with the thin baked consolidated ash layer. The lower segment, which starts from the bottom of the outcrop, has maximum and average thicknesses of 32 cm and 23 cm, respectively. The segment ranges in dip from vertical, in the lower part, to 80° toward NW at its top.

4.2. Petrographic and major elements analyses of the dikes

Based on petrographic and geochemical analyses, the dikes are of sub-alkaline basalts, based on the total alkali-silica diagram (Le Maitre et al., 2002), and their compositions overlap with the bulk rock compositions of the RP magmatic systems (Jakobsson et al., 1978; Gurenko et al., 1990; Sinton et al., 2005; Kokfelt et al., 2006; Peate et al., 2009; Koornneef et al., 2012; Fowler and Zierenberg, 2016a, 2016b; Bindeman et al., 2022; Halldórsson et al., 2022). Both dikes show a tholeiitic affinity in the AFM diagram (chemical analyses of whole rocks of this study are provided in *Appendix file A1*). The Younger Stampar dikes show lower MgO concentrations than the other historical lavas on the RP, suggesting that the dikes have undergone higher degrees of crystallisation (Fig. 7). The K_2O/TiO_2 ratio of the studied dikes increases as the MgO content decreases, suggesting the crystallisation of Ti-magnetite. The K_2O/TiO_2 ratio has been used in the literature to assess different magmatic sources in Iceland. The studied Younger Stampar dikes are consistent with the MgO versus K_2O/TiO_2 trend defined by most of the historical lavas at Reykjanes Peninsula (Fig. 7), with the exception of the 2021 Fagradalsfjall lavas (Bindeman et al., 2022; Halldórsson et al., 2022) where there was a systematic increase of K_2O/TiO_2 and MgO during the eruption which, together with other geochemical signals, is interpreted as being the result of mixing of mantle magmas.

All the studied thin sections show porphyritic textures. In the groundmass of the arrested sample, we observe microphenocrysts of plagioclase, clinopyroxene and Ti-magnetite showing from skeletal (clinopyroxene and plagioclase) to dendritic (Ti-magnetite and clinopyroxene) morphology immersed in glass (Figs. 8C-D). In contrast, the groundmass of the feeder dike consists of plagioclase and clinopyroxene microphenocrysts with polyhedral morphology, and Ti-magnetite showing from skeletal to dendritic morphology (Figs. 8A-B). Thus, the different groundmass textures of the two dikes suggest that the arrested dike underwent a faster cooling than the feeder dike.

The modal composition of the studied basalts correlates with the dike paths. In fact, the modal composition of the two samples from the arrested dike (53A and 53B) is 6% and 8% for the plagioclase crystals, respectively, 1% for the clinopyroxenes and <1% for the olivines. The feeder dike samples (51A and 51B) show 2% and 3% plagioclase

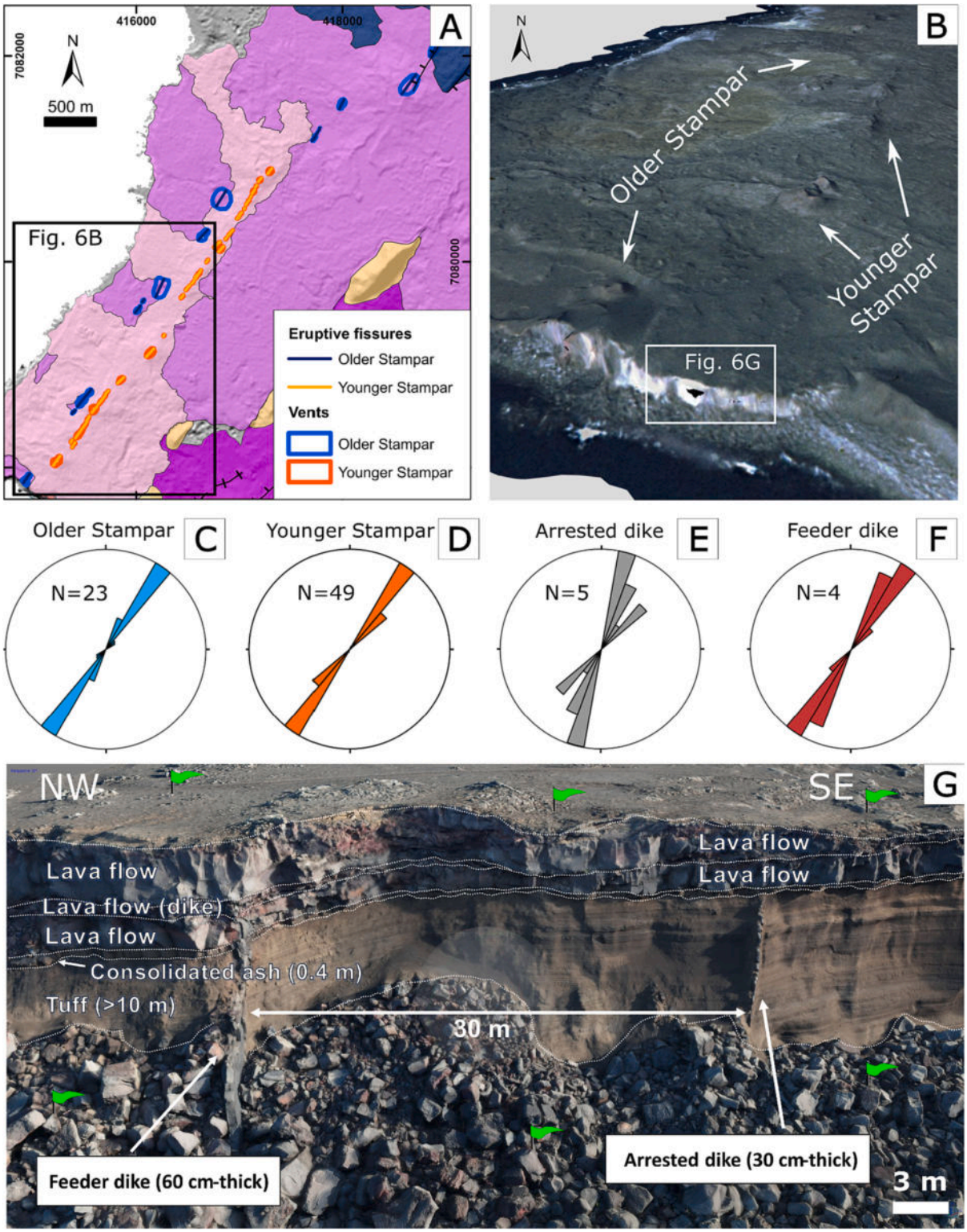

Fig. 6. A) Detailed map of the Older and Younger Stampar crater rows, with the strike of the eruptive fissures inferred by the elongation of each vent. For lava units, see the legend in Fig. 2A. Spatial reference: WGS 84 – UTM zone 27 N. B) View of the 3D model obtained from historical aerial photographs (location in Fig. 6A), where the absence of tension fractures and faults can be noticed. Rose diagrams showing the strike of C) the Older Stampar eruptive fissures, D) the Younger Stampar eruptive fissures, and of the outcropping segments of E) the arrested and F) the feeder dike. G) UAV-derived 3D model of the outcrop, with the layers and the two dikes highlighted (location in Fig. 6B). Ground Control Points (GCPs) used to georeference the model are shown as green flags. (For interpretation of the references to colour in this figure legend, the reader is referred to the web version of this article.)

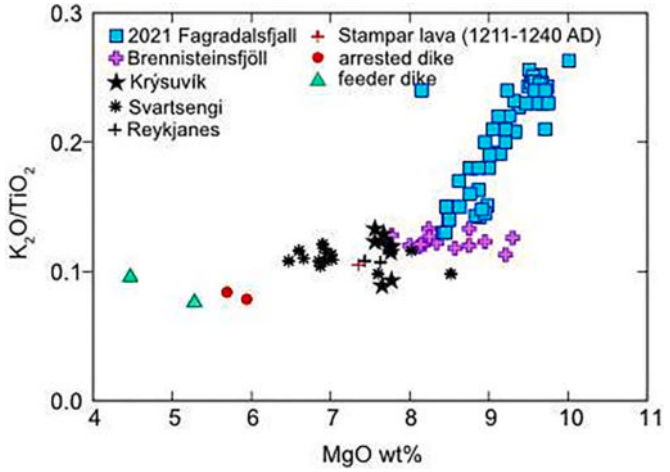

Fig. 7. MgO versus K_2O/TiO_2 of bulk rocks of the Younger Stampar dikes compared with historical lavas of the RP. Bulk rock data from historical lavas are from the literature. Bulk rock data: 2021 Fagradalsfjall (Bindeman et al., 2022; Halldórsson et al., 2022), Brennisteinsfjoll (Sinton et al., 2005; Kokfelt et al., 2006; Peate et al., 2009), Krisuvik (Peate et al., 2009; Koornneef et al., 2012), Svartsengi (Gee et al., 1998; Kokfelt et al., 2006; Peate et al., 2009; Koornneef et al., 2012), Reykjanes (Peate et al., 2009; Koornneef et al., 2012). Notice the lower MgO content of the bulk rocks of the Younger Stampar dikes relative to the bulk rock of a Stampar 1211–1240 CE lava (red cross symbol; data by Peate et al., 2009). (For interpretation of the references to colour in this figure legend, the reader is referred to the web version of this article.)

crystals, respectively, 1% clinopyroxenes, while olivine is rare in one sample (51A) and absent in the other (51B). The higher porphyritic index of the arrested dike is in agreement with the field observations reported by Gudmundsson (2017, see chapter 13).

In all the thin sections, plagioclase is the most abundant phenocryst, followed by phenocrysts of clinopyroxene and olivine. Plagioclase and clinopyroxene crystals are commonly observed as glomerocrysts. Plagioclase phenocrysts are from 0.5 to 2 mm in size and are generally larger than clinopyroxenes and olivines independently of the dike type. Most of the phenocrysts bear slightly to strongly crystallised melt inclusions, but no fluid inclusions were observed in any of the phenocrysts, suggesting they were growing in a volatile undersaturated magma (Esposito, 2021). The degrees of crystallisation of melt inclusions roughly correlates with their size. Twenty-five plagioclase phenocrysts were analysed in the core and the rim and span a wide range of compositions (Fig. 9A). In particular, the plagioclases of the arrested dike show $An_{89–70}$ while those of the feeder dike show $An_{81–71}$. Plagioclase in the groundmass has a narrower range of anorthite composition. In particular, the arrested dike shows $An_{71–68}$ with an outlier of An_{52}, and the feeder dike shows $An_{69–60}$. Most of the analysed plagioclase phenocrysts are normally zoned or unzoned. However, two of the plagioclase phenocrysts in the arrested dike show a strongly reversely zoned rim from An_{72} in the core to An_{84} and An_{79} in the rim, respectively (*Appendix file A1*). This same reverse zonation is not observed for plagioclase phenocrysts found in the feeder dike. While these plagioclase compositions partially overlap, there is correlation between the highest An contents of a single sample with the corresponding Mg# based on the whole rock analysis (Fig. 9A). The mineral chemistry is consistent with the bulk rock analysis and as the Mg# decreases, the highest An content of plagioclase decreases. The An content versus the Mg# of the whole rock of the studied samples (both feeder and arrested) is in trend with the compositions of the RP historic lavas reported by Peate et al. (2009).

Pyroxenes are found in glomerocrysts associated with plagioclase in all the studied four samples and have augitic composition based on the pyroxene quadrilateral by Morimoto (1988) (Fig. 9B). Even though limited preliminary data is available for clinopyroxene phenocrysts (4 clinopyroxenes of the arrested and 3 clinopyroxenes for the feeder), they cluster in a limited field of the quadrilateral. Clinopyroxene phenocrysts

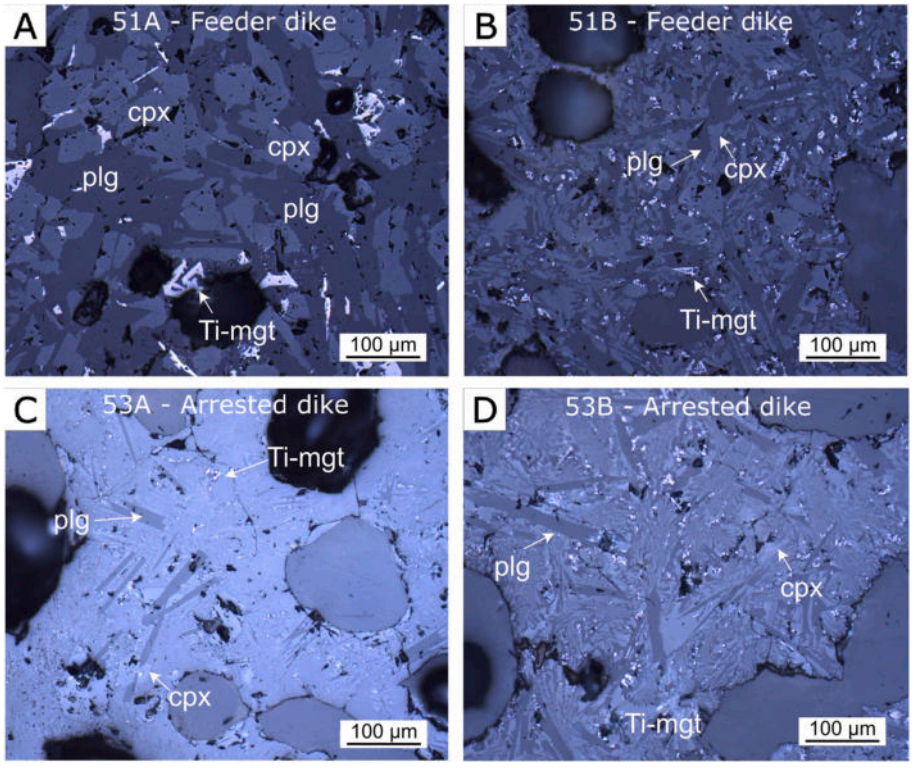

Fig. 8. Photomicrographs of the dikes' groundmass collected using reflected light. A-B) photomicrographs of the feeder dike samples (51 A and B); C-D) photomicrographs of the arrested dike samples (53 A and B).

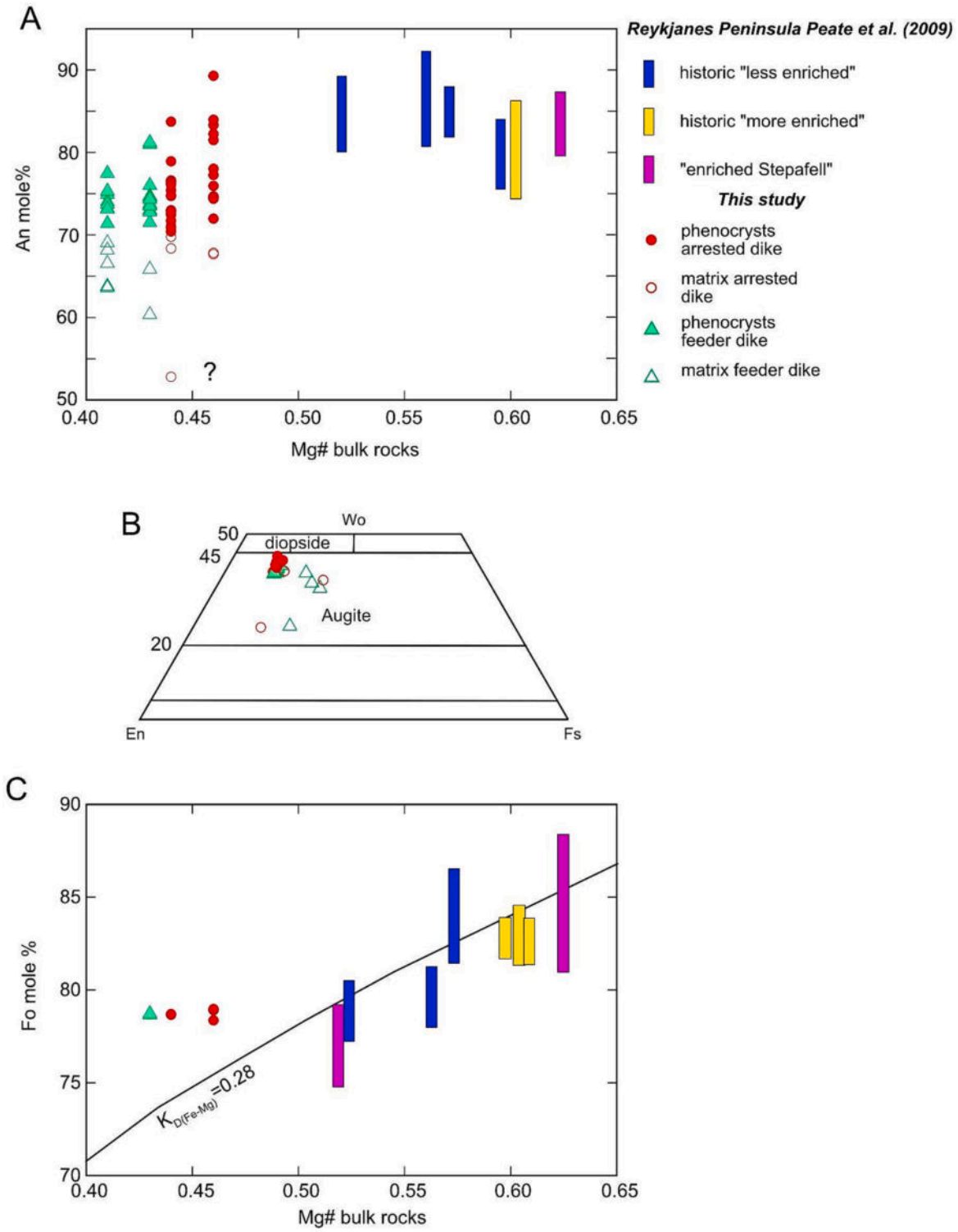

Fig. 9. Mineral composition of the samples studied compared to data from Peate et al. (2009). A) An mole% of plagioclase versus the Mg# of the corresponding whole rock. Notice the correlation between the maximum An content and the Mg# of the corresponding whole rock. The question mark denotes an outlier data point. B) pyroxene quadrilateral (Morimoto, 1988). The Fs component of pyroxenes of the groundmass is characterised by higher contents relative to the pyroxene phenocrysts. C) Fo mole% of olivine versus the Mg# of the corresponding bulk rocks. The line represents the partition coefficient of Fe-Mg between the silicate liquid (as whole rock) and olivine of 0.28, representing the lowest value possible for these systems as calculated by Peate et al. (2009). The Fo mole% of olivines of the studied sample show a narrow range. The Mg# in A) and C) is calculated as $Mg/(Mg/Fe^{2+})$ with $Fe_2O{=}FeO_{tot}{*}0.86$.

of the feeder dike show Wo contents toward lower values ($En_{49–46}$, Fs_{12}, $Wo_{41–39}$) relative to those of the arrested dike ($En_{49–45}$, $Fs_{12–10}$, $Wo_{40–44}$). As for plagioclase phenocrysts, pyroxenes were analysed both in the core and in the rim, but no significant chemical zoning was detected. Clinopyroxenes from the groundamass show significantly lower Wo and trend toward higher Fs and En components ($En_{59–38}$, $Fs_{24–14}$, $Wo_{40–25}$) relative to clinopyroxene phenocrysts independently on the dike type (*Appendix file A1*).

Rare olivine crystals were observed in thin sections and were analysed for major elements using the EDAX method. Olivines were between 0.5 and 1 mm and were found as single crystals. The calculated Fo content is 79 mol% independently on the type of the dike (Fig. 9C). The Fo content of the olivines suggests that they may not be in equilibrium with the host magma. In fact, the $K_{D(Fe—Mg)}$ between silicate liquid (as whole rock) and olivine shows inconsistent low values (Fig. 9C). The composition of the studied olivine is comparable with the lavas showing lower Mg# studied by Peate et al. (2009). Based on the preliminary data of mineral chemistry, bulk rocks and modal composition, it is suggested that the two dikes show some significant differences, as summarised in Table 1.

4.3. Numerical modelling

4.3.1. Setting I

In setting I, we modelled the arrested dike with an overpressure from 2 to 4 MPa. When the dike is at the depth Y_1 (Figs. 10D-E-F), regardless of its overpressure, σ_1 is vertical and σ_3 is horizontal at the dike tip, so the dike is likely to propagate to the surface. When we increase the dike overpressure, the tensile and von Mises shear stresses at the surface also increase from 2.8 MPa to 5 MPa and from 2.45 MPa to 4.9 MPa, respectively (Figs. 10A-B-C). However, in the first two models the von Mises stress concentration is not high enough to form faults (Figs. 10A-B). Instead, the tensile stress concentration at the surface indicates likely tension fractures.

Moving the dike to a shallower depth, Y_2 (Figs. 10J-K-L), we observe no rotation of the principal stresses at the tip, regardless of the overpressure. Increasing the overpressure, the tensile and von Mises stresses at the surface increase from 3.4 to 6.6 MPa and from 3 to 6 MPa, respectively (Figs. 10G-H-I). When the overpressure is 2 MPa, the von Mises stress is too low to form faults at the surface (Fig. 10G), whereas tensile stress concentration suggests that tension fracturing is likely in all the models.

If the dike is modelled at Y_3 depth (Figs. 10P-Q-R) no rotation of the principal stresses is observed at the tip, indicating the likely propagation of the dike to the surface. When we increase the dike overpressure, the tensile and von Mises stresses at the surface increase from 4.5 MPa to 9.1 MPa and from 4.1 MPa to 8.1 MPa, respectively (Figs. 10M-N-O). In all the models, the concentration of stresses at the surface indicates likely fracturing and faulting. In all the models, we notice that propagating the dike closer to the tuff-lava contact, the concentration of tensile stress at the dike tip decreases, while it increases within the upper lava layers. This is because part of the potential tip stresses is transferred to the much stiffer lava flow, as commonly observed in numerical models (Inskip et al., 2020).

In Fig. 11, we model the arrested dike with an overpressure from 2 MPa to 4 MPa and a 1 MPa extensional stress field (applied as in Fig. 5A). When the dike is at the depth Y_1 (Figs. 11D-E-F), regardless of its overpressure, σ_1 is vertical and σ_3 is horizontal at the dike tip, indicating the likely propagation of the dike to the surface. Increasing the overpressure, the tensile and von Mises stresses increase from 5.5 MPa to 8.1 MPa and from 4.8 MPa to 7.4 MPa, respectively (Figs. 11A-B-C). The concentration of stresses at the surface indicates that fracturing and faulting are likely in all the models.

Moving the dike tip upwards at Y_2 depth (Figs. 11J-K-L) and at Y_3 depth (Figs. 11P-Q-R), no principal stress rotations occur at the tip. When we increase the dike overpressure, the tensile and von Mises stresses at the surface increase from 6.1 MPa to 9.5 MPa and from 5.5 MPa to 8.5 MPa, respectively (dike tip at the depth Y_2) (Figs. 11G-H-I), and from 7.4 MPa to 11.5 MPa and from 6.5 MPa to 10.6 MPa, respectively (dike tip at depth Y_3) (Figs. 11M-N-O). These concentrations of stresses at the surface suggest that fracturing and faulting are expected. In all the models, moving the dike closer to the tuff-lava contact, tensile stress at the dike tip decreases while it increases within the upper lava layers, for the reasons explained above.

4.3.2. Setting II

In setting II we modelled the arrested dike subject to a constant overpressure of 3 MPa and an extension of 1 MPa. In Fig. 12 we show the role of tuff stiffness. At depth Y_1, there is no rotation of the principal stresses, regardless of E (Young's modulus) values of the tuff (Figs. 12D-E-F). When we increase E, tensile stress magnitudes increase from a maximum of 6–8 MPa at the tip of the dike (Fig. 12D), to 10–12 MPa (Fig. 12E), and finally to 14–16 MPa (Fig. 12F), while absolute shear stress contours form greater lobes in the tuff (Figs. 12D-E-F). In all the models, the von Mises and tensile stresses at the surface are >4 and 2 MPa, respectively, so both fracturing and faulting are likely to occur.

In the next round of models, the dike tip is at depth Y_2 (Figs. 12J-K-L). The results show that regardless of the tuff stiffness, no rotation of principal stresses is observed. On increasing the stiffness of the tuff layer the tensile stress magnitudes at the tip increase, from 6–8 MPa (Fig. 12J), to 10–12 MPa (Fig. 12K), and finally to 14–16 MPa (Fig. 12L). Absolute shear stress contours form larger lobes as well (Figs. 12J-K-L). The stresses at the surface are great enough to generate fracturing and faulting.

Moving the dike tip to depth Y_3, if we also increase the E of the tuff layer no stress rotation is observed (Figs. 12P-Q-R), but tensile stress increases in the consolidated ash layer and lower lava layers, up to 16–18 MPa (Fig. 12R). Absolute shear stress contours get closer to the surface (Figs. 12P-Q-R). At the surface, tensile stress magnitudes increase from 9.5 MPa (Fig. 12M), to 10.2 MPa (Fig. 12N), and finally to 10.4 MPa (Fig. 12O), suggesting fracturing. Von Mises stress increases from 8.6 MPa (Fig. 12M), to 9.3 MPa (Fig. 12N), and finally to 9.4 MPa (Fig. 12O), indicating that faulting is likely at the surface.

In Fig. 13, we investigate the role of lava stiffness. At depth Y_1, regardless of E values, we do not observe a rotation of the principal stresses (Figs. 13C-D). However, tensile stress concentrates in the lava layer with greater E value, namely the upper one (UL) in Fig. 13C, and the lower one (LL) in Fig. 13D. When E_{UL} is greater than E_{LL} (Fig. 13A), the tensile and von Mises concentrations at the surface are 9.8 MPa and 8.8 MPa, respectively. When E_{UL} is smaller than E_{LL} (Fig. 13B), stresses at the surface are up to 4.7 MPa and 4.2 MPa.

In the models with dike tip at depth Y_2, tensile stress always tends to concentrate in the lava with greater E (Fig. 13G-H). When E_{UL} is greater than E_{LL}, there is an increase in concentrations of tensile and von Mises stresses at the surface (up to 11.3 and 10.2 MPa, respectively) (Fig. 13E). When E_{UL} is smaller than E_{LL}, there is less concentration of stresses at the surface (up to 5.4 and 4.8 MPa, respectively) (Fig. 13F).

When the dike tip is at depth Y_3, tensile stress is more concentrated in the upper lava layer when E_{UL} is greater than E_{LL} (Fig. 13K), and in the lower lava layer when E_{UL} is smaller than E_{LL} (Fig. 13L). At the surface, tensile and von Mises stresses are up to 13.9 MPa and 12.6 MPa when the upper lava layer is stiffer (Fig. 13I), whereas they are up to 6.6 and 6 MPa, respectively, where the upper lava is softer or more compliant (Fig. 13J).

In all the models, concentrations of stresses at the surface indicate fracturing and faulting. Regardless of the value of E of the tuff and lava

Table 1
Petrographic and geochemical differences between the feeder and the arrested dikes. Mg# = Mg/(Mg + Fe^{2+}) assuming Fe_2O=FeO_{tot}*0.86.

Dike type	% phenocrysts	phenocryst type	Anorthite in plg cores (mole%)	type of zonation in plg	Mg#	SiO_2 wt%
Feeder	2 to 4	Plg, ±oli, cpx	81–71	normal	0.41–0.43	48.76–48.81
Arrested	7 to 9	Plg, oli, cpx	89–70	inverse and normal	0.44–0.46	46.32–48.17

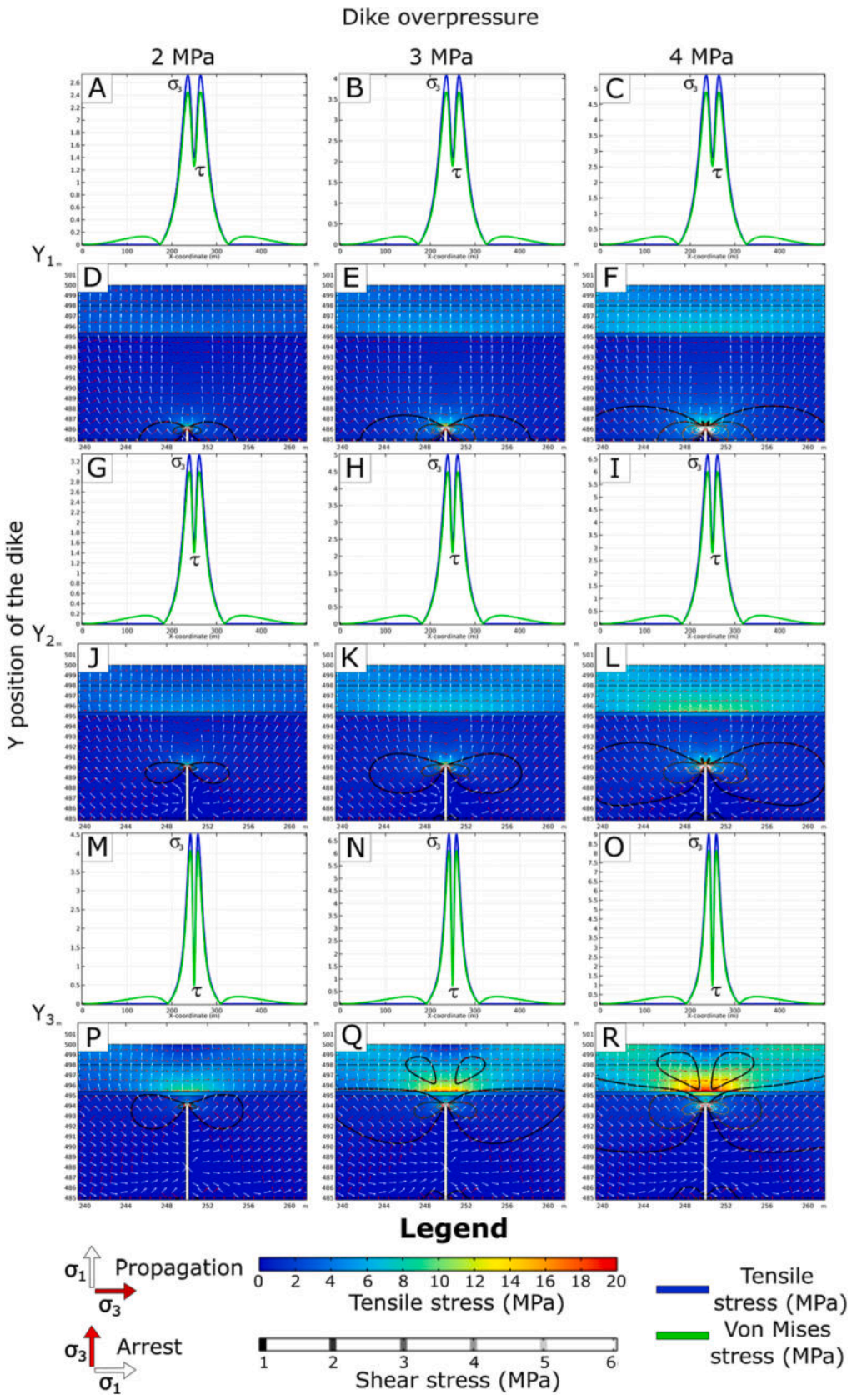

Fig. 10. Numerical models with the dike located at different depths (Y_1, Y_2, Y_3) and with varying overpressure values (2 MPa to 4 MPa). The distribution of tensile stress (σ_3) is shown with the colour scale bar, while the absolute shear stress (τ) (von Mises component in xy plane) is represented with contour lines. The trajectories of σ_1 and σ_3 are shown by white and red arrows, respectively. The 1D graphs show tensile (σ_3, blue line) and von Mises (τ, green line) stresses at the surface. (For interpretation of the references to colour in this figure legend, the reader is referred to the web version of this article.)

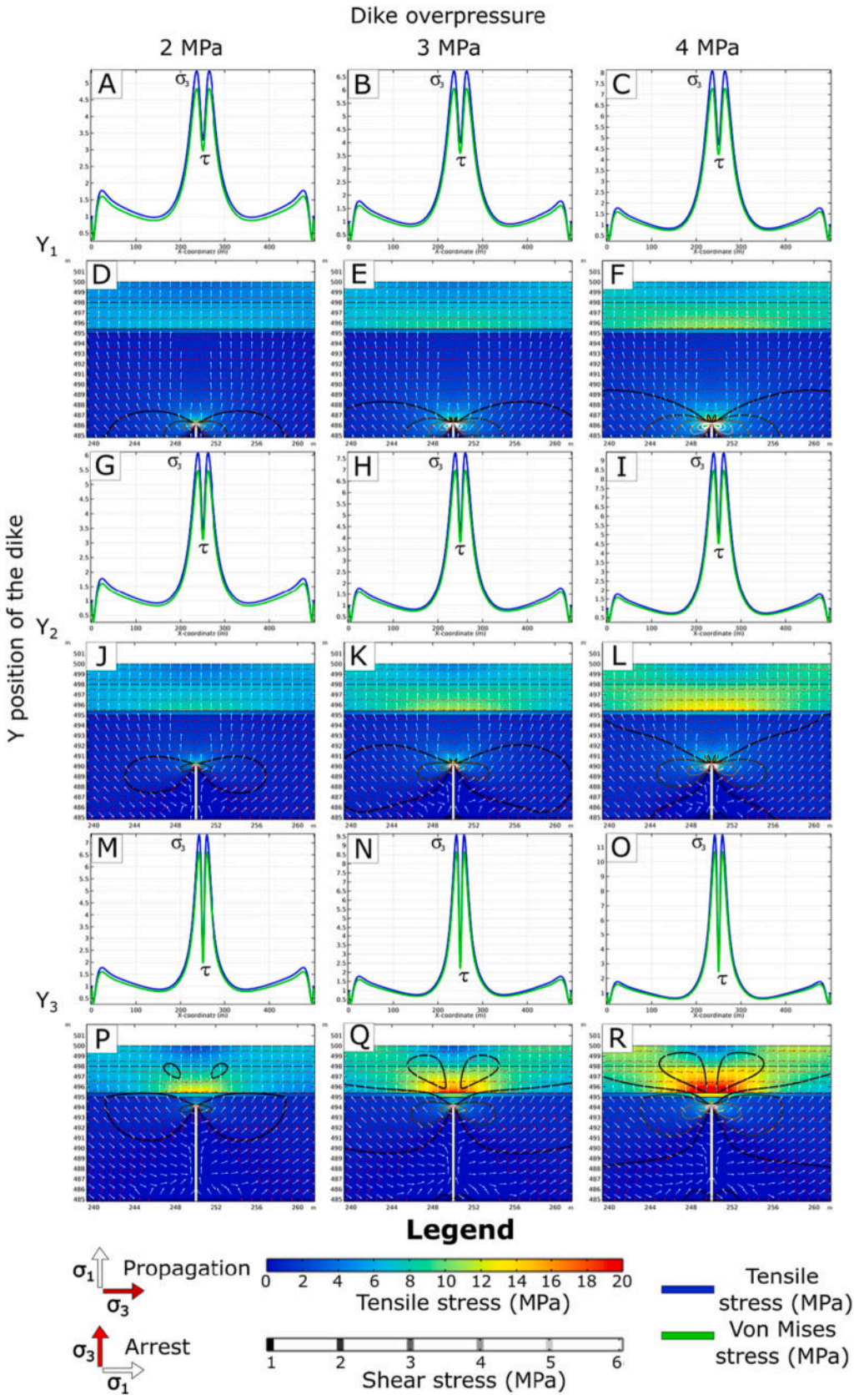

Fig. 11. Numerical models with the dike tip located at different depths (Y_1, Y_2, Y_3) and with varying overpressure values (2 MPa to 4 MPa). In all the models, a 1 MPa extensional stress field is applied. The distribution of tensile stress (σ_3) is shown with the colour scale bar, while the absolute shear stress (τ) (von Mises component in xy plane) is represented with contour lines. Trajectories of σ_1 and σ_3 are shown by white and red arrows, respectively. The 1D graphs show tensile (σ_3, blue line) and von Mises (τ, green line) stresses at the surface. (For interpretation of the references to colour in this figure legend, the reader is referred to the web version of this article.)

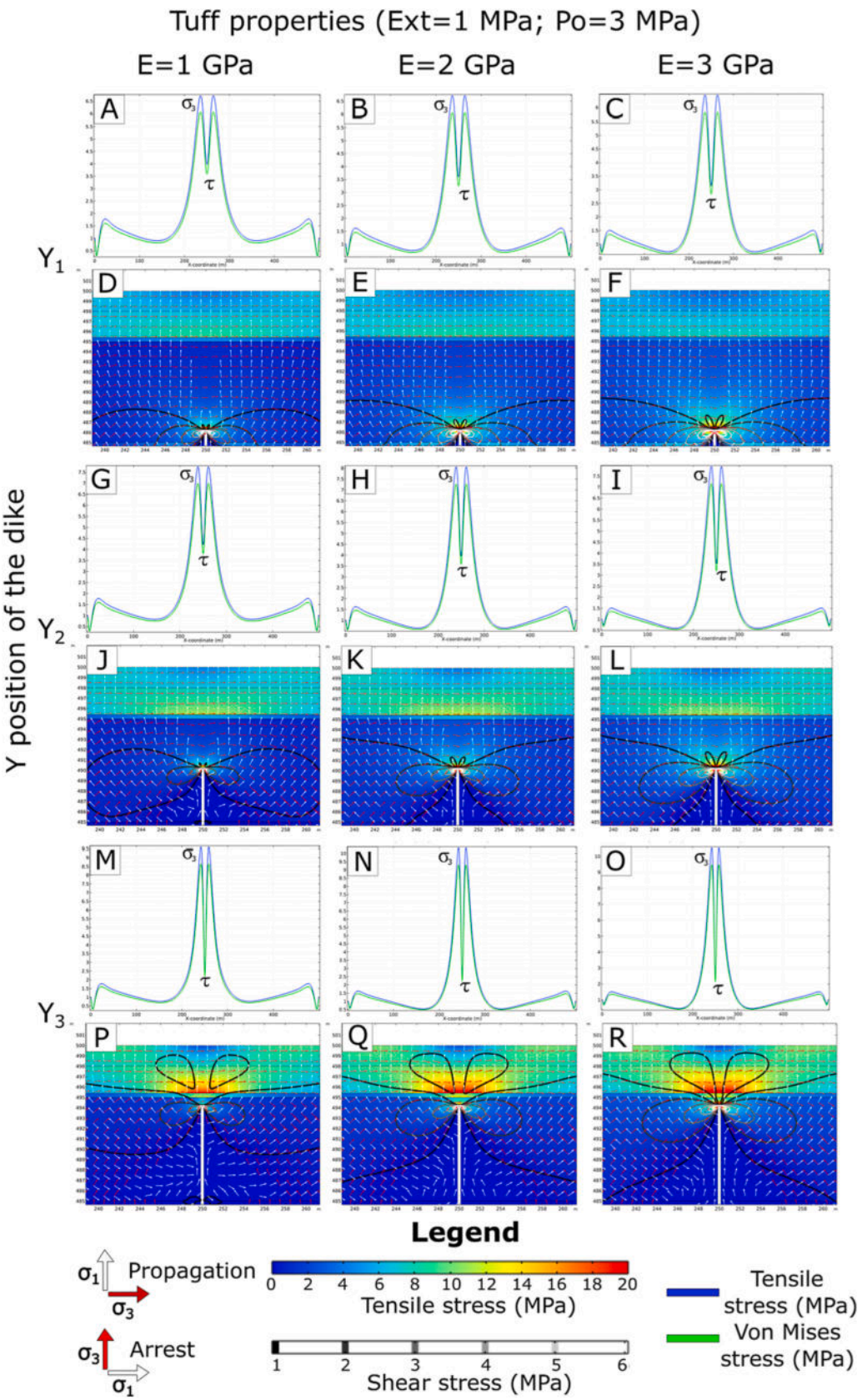

Fig. 12. Numerical models with the dike tip located at different depths (Y_1, Y_2, Y_3) and with varying values of Young's modulus of the tuff (1 to 3 GPa). In all the models, an overpressure of 3 MPa and a 1 MPa extensional stress field are applied. The magnitude of the tensile stress (σ_3) is shown with the colour scale bar, while the absolute shear stress (τ) (von Mises component in xy plane) is represented with contour lines. The trajectories of σ_1 and σ_3 are shown by white and red arrows, respectively. The 1D graphs show tensile (σ_3, blue line) and von Mises (τ, green line) stresses at the surface. (For interpretation of the references to colour in this figure legend, the reader is referred to the web version of this article.)

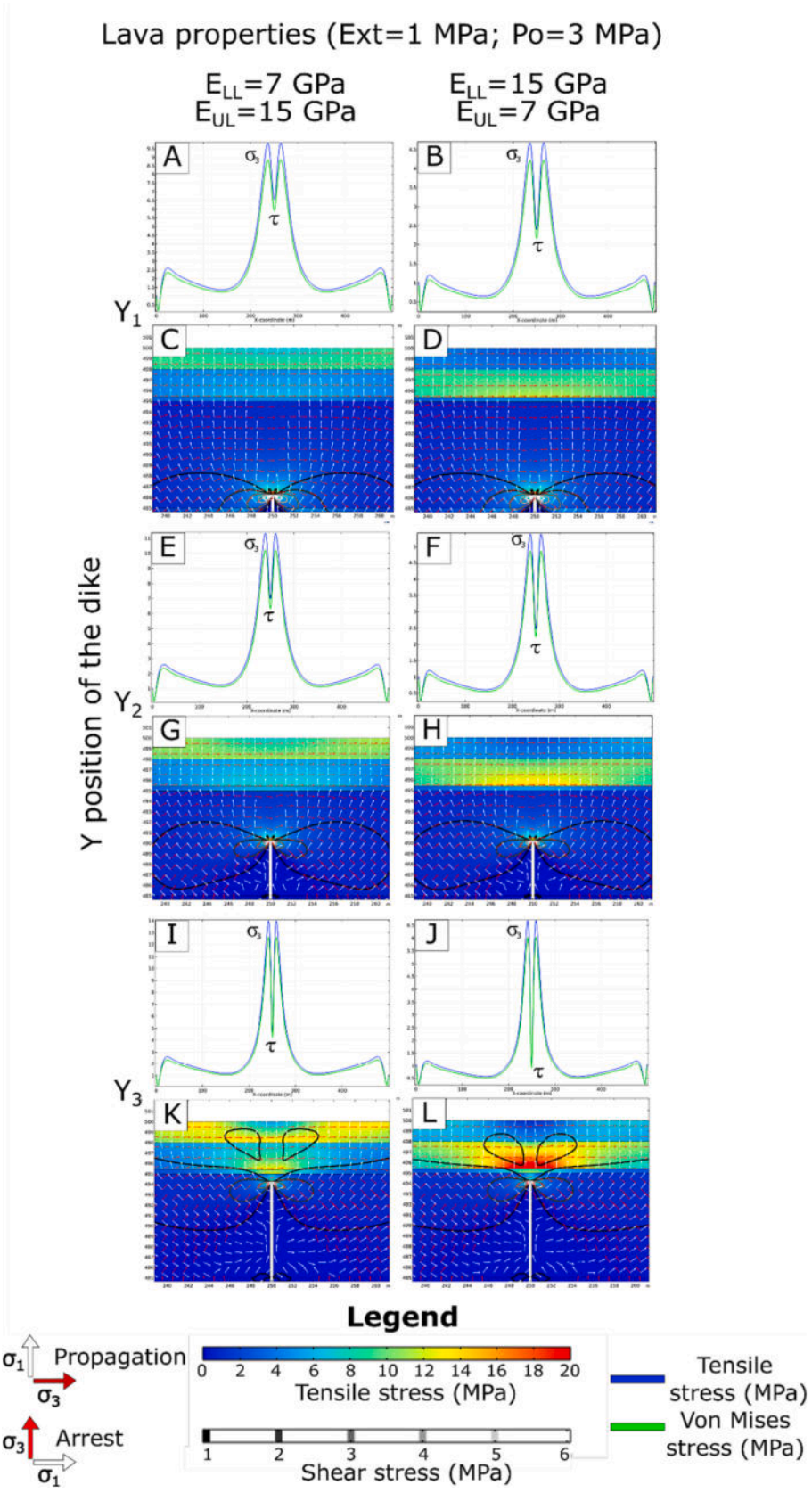

Fig. 13. Numerical models with the dike tip located at different depths (Y_1, Y_2, Y_3) and with different values of E for the lava layers. In all models, an overpressure of 3 MPa and a 1 MPa extensional stress field are applied. The distribution of tensile stress (σ_3) is shown with the colour scale bar, while the absolute shear stress (τ) (von Mises component in xy plane) is represented with contour lines. The trajectories of σ_1 and σ_3 are shown by white and red arrows, respectively. The 1D graphs show tensile (σ_3, blue line) and von Mises (τ, green line) stresses at the surface. (For interpretation of the references to colour in this figure legend, the reader is referred to the web version of this article.)

layers, moving the dike closer to the tuff-lava contact the tensile stress at the tip decreases, and it increases in the upper lava layers (Figs. 12-13).

4.3.3. Setting III

In setting III, we evaluated the influence of the horizontal compression due to a previous intrusion, that of the feeder dike (Gudmundsson, 2017). In Fig. 14, we show that the feeder dike cut the tuff, the thin consolidated ash layer, and the lower lava layer, before reaching the topographic surface at that time to generate a new lava flow (as observed also in Fig. 6G). The overpressure of the feeder dike caused a horizontal compression in the host rock that could have affected the nearby arrested dike which was intruded later (Fig. 14) (Gudmundsson, 2003; Menand et al., 2010).

In Fig. 15, we model the arrested dike subject to an overpressure of 2–4 MPa and a horizontal compressive stress of 1–4 MPa (as shown in Fig. 5C). When the compressive stress is equal to 1 MPa (Figs. 15A-B-C) then, regardless of the dike overpressure, σ_1 and σ_3 rotations are <90°, but up to 45°. Tensile stress concentration in the lavas reaches 5–6 MPa when the overpressure is 4 MPa, indicating possible fracturing (Fig. 15C).

Applying a compressive stress of 2 MPa (Figs. 15D-E-F), we observe a 90° rotation of the principal stresses ahead of the dike tip when the dike overpressure is 2 MPa (Fig. 15D). By contrast, when dike overpressure increases to 3 MPa (Fig. 15E) and 4 MPa (Fig. 15F) stress rotations are up to 80° and 60°, respectively. However, tensile stress concentrations at the tip and in the lava layers are <2–3 MPa, indicating that fracturing is unlikely.

Increasing the compressive stress to 3 MPa (Figs. 15G-H-I), there is a 90° rotation of the principal stresses with dike overpressures of 2 (Fig. 15G) and 3 MPa (Fig. 15H), whereas a 80° rotation occurs with a dike overpressure of 4 MPa (Fig. 15I). Absolute shear and tensile stress concentrations at the tip and within the lava layers decrease as well.

When the applied compressive stress is 4 MPa (Figs. 15J-K-L), then, regardless of the dike overpressure, there is a 90° rotation of the principal stresses, indicating a likely arrest of the dike. Absolute shear and tensile stress concentrations also decrease at the tip and in the lava layers.

4.3.4. Synthesis of the numerical models

In Table 2 we summarise the influence of the modelled parameters on dike propagation and arrest. Our models show that dike arrest is likely to occur when the overpressure and the tensile stress decreases at the tip of the dike (Figs. 10-11). For the present dikes, stress barriers do not form solely because of abrupt changes in the mechanical properties (stiffness) between layers. If the dike is moved closer to the contact between a soft (tuff) and a stiff (lava) layer, however, the tensile stress decreases in the soft layer and increases in the stiff layer (Figs. 10-11-12-13). Similarly, when local horizontal compressive stress is applied (here due to the earlier emplaced feeder dike) in the layer ahead of a dike tip, the tensile tip stress also decreases (Fig. 15). Generally, whenever compressive stress in a layer or unit ahead of dike tip is equal to or greater than dike overpressure, the resulting stress barrier encourages dike arrest (Fig. 15). The suppression of tensile and shear stress around the dike tip as it approaches a stress barrier is the main reason for the absence of dike-induced fracturing at the surface.

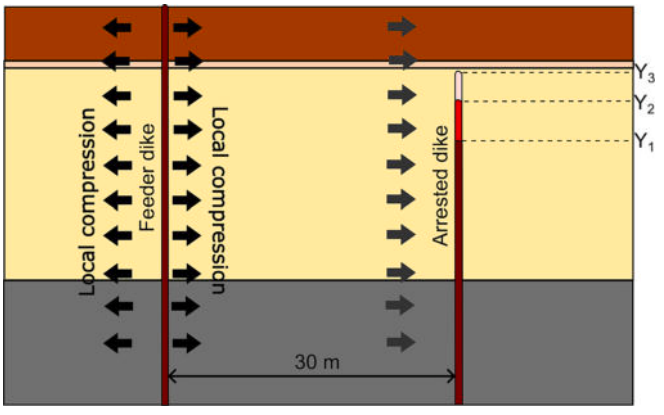

Fig. 14. Conceptual model. The feeder dike intruded the observed stratigraphy and induced local horizontal compression that contributed to the arrest of the (later injected) arrested dike.

5. Discussion

In the RP, the most recent rifting episode is represented by the unrest in the Fagradalsfjall system, which has been going on since mid-December 2019, with periods of high seismicity associated with repeated dike-segment intrusions (Sigmundsson et al., 2022). However, until June 2023, only two dike-segments managed to propagate up to the surface, leading to two eruptive events. Before the Fagradalsfjall eruption, the latest episode in the RP occurred between 1210 and 1240 CE, and included the Younger Stampar eruption (Saemundsson et al., 2016, 2020, Fig. 1).

Our structural results indicate that the average strike of the Younger Stampar eruptive fissure is N38.8°E, which is similar to that of the Older Stampar fissure (N33.2°E), with a predominance of NNE-NE strike for both (Figs. 6C-D). These strike values are consistent with the average orientation of the eruptive fissures associated with other historical and prehistoric eruptions on the RP (commonly about N40°E), as highlighted in Fig. 1 (Clifton and Schlische, 2003; Clifton and Kattenhorn, 2006; Saemundsson et al., 2016). This strike is also consistent with the 2021–2022 Fagradalsfjall eruptive fissures, which have two segments, the northern striking N45°E and the southern N25°E (Barsotti et al., 2023; Flóvenz et al., 2022; Sigmundsson et al., 2022). All these fissures are parallel to the orientation of the main structures of the volcanic systems in the peninsula, which are arranged en-échelon relative to the plate boundary. Structures within these volcanic systems have a mean orientation ranging between N21°E and N60°E (Clifton and Schlische, 2003; Clifton and Kattenhorn, 2006). The RP trends about N70°E in the western part and about N80°E in the eastern part (Gudmundsson, 1986b, 1987), oblique to the spreading direction in this region (N101°E, DeMets et al., 2010), forming a transtensional zone. The strike of the dike segments is also similar to those of the Younger Stampar fissure orientation.

Petrographic and geochemical analyses of the rocks representing the two dikes under study suggest that the feeder dike is crystal-poor and slightly more evolved (lower MgO, Mg# and higher SiO_2) than the arrested one (Table 1). As suggested by the petrographical and geochemical affinities of both dikes, we can assume that the source of the two dikes is the same. Based on this assumption, the lower Mg# of the feeder dike indicates that the magma of that dike must have been cooler than the arrested one. Using the software Petrolog3 (Danyushevsky and Plechov, 2011) and assuming sample 53A as the starting composition, then the liquidus temperature of a magma with MgO = 6.01 wt% corresponds to 1199 °C. The temperature of such magma would decrease to 1067 °C after 9% crystallisation (see *Appendix file A2* for the parameters assumed for this fractional crystallisation model). The same magma differentiating by 30% crystal fractionation gives 5.27 wt% of MgO (MgO of sample 51B = 5.28 wt%) and a temperature of 1107 °C. The petrographic observations and Petrolog model predict the crystallisation of only anhydrous phases (plagioclase, olivine and clinopyroxene, spinel). Assuming a starting H_2O concentration of 0.2 wt% (Halldórsson et al., 2022), the H_2O content of the magma associated with the feeder dike could have been 0.29 wt%, enriched by 0.09 wt% relative to the magma associated with the arrested dike. The higher volatile contents and the lower amount of crystals suggest that the magma of the feeder dike may have been less viscous than the arrested one (Spera, 2000). Another important preliminary result of this study is

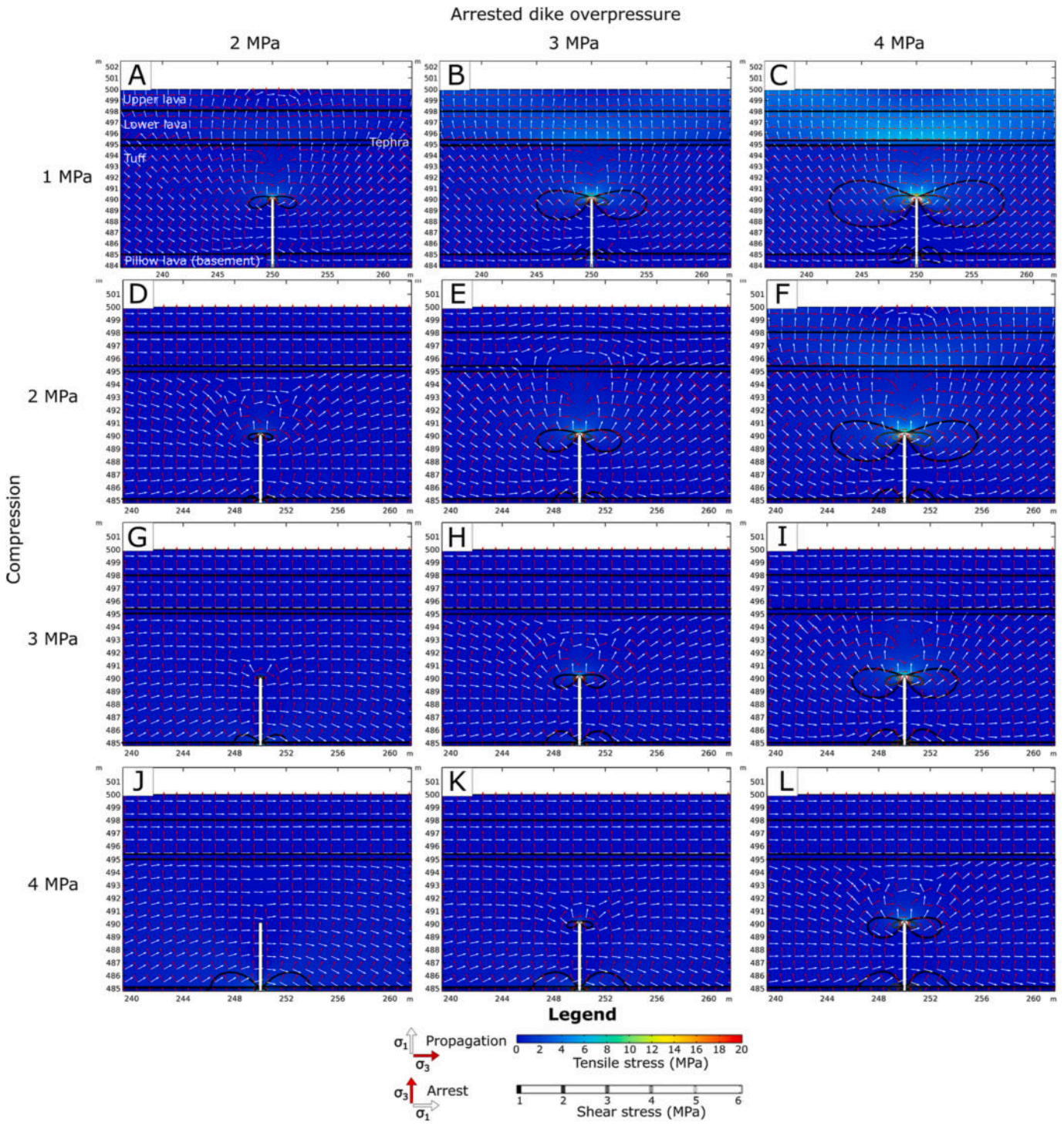

Fig. 15. Numerical models with the dike tip located at depth Y_2 and with different overpressure values (2 MPa to 4 MPa). A horizontal compressive stress (1 MPa to 4 MPa) is applied as shown in Fig. 5C. The distribution of tensile stress (σ_3) is shown with the colour scale bar, while the absolute shear stress (τ) (von Mises component in xy plane) is represented with contour lines. The trajectories of σ_1 and σ_3 are shown by white and red arrows, respectively. (For interpretation of the references to colour in this figure legend, the reader is referred to the web version of this article.)

the plagioclase reverse zoning observed in the arrested dike. Particularly in one sample (53A), a plagioclase core shows An_{72} and the rim shows An_{84} (see *Appendix File A1*). The plagioclase reverse zoning at the rim may indicate that the magma of the arrested dike had gone through a magmatic process such as magma mixing with deeper-hotter less evolved magma before eruption (e.g., Putirka, 2017 and references therein; Esposito et al., 2018 and references therein) or crystal settling in a chemically layered magma reservoir (e.g., Anderson et al., 2000). Petrological and petrographical modelling will be the subject of further studies based on melt inclusions, in addition to whole rock and mineral data.

Over the past decades, much research based on numerical models has been carried out regarding the factors that can affect dike propagation (e.g., Gudmundsson, 2003; Maccaferri et al., 2010, 2011, 2016; Geshi et al., 2012; Philipp et al., 2013; Barnett and Gudmundsson, 2014; Rivalta et al., 2015; Urbani et al., 2017; Drymoni et al., 2020, 2023;

Table 2
Synthesis of the results of numerical models, showing the influence of the modelled parameters on the formation of stress barriers and on the decrease of stresses at the tip of the dike.

Modelled parameter	Stress barrier	Stress decrease at the tip
Dike overpressure	No	Yes
Layers' mechanical parameters (Young's modulus)	No	Yes
Compression < dike overpressure	No	Yes
Compression ≥ dike overpressure	Yes	Yes

Tibaldi et al., 2022). Dike arrest or deflection into a sill may occur because of stress barriers, namely layers or units where the local stress field is unfavourable to dike propagation (Gretener, 1969; Gudmundsson, 1986a). Elastic mismatch, where there is a strong contrast in Young's modulus across a contact between the layer below the contact and hosting the dike and the layer above the contact, can also represent a mechanism of dike arrest (Gudmundsson, 2011b). In our numerical models, we have explored the influence of the following factors on dike propagation: i) dike overpressure; ii) layer's mechanical properties (Young's modulus or stiffness), and iii) presence of an extensional or compressional tectonic stress field.

When overpressure decreases, tensile stress concentration at the tip of the dike decreases, inhibiting dike propagation. This is coherent with Drymoni et al. (2023), who showed that, in low overpressure conditions, dike arrest is likely, and with Geshi et al. (2012) and Drymoni et al. (2020), who discuss further the effects of magmatic overpressure on dike propagation.

Previous numerical studies (e.g., Al Shehri and Gudmundsson, 2018; Drymoni et al., 2023) indicate that most dikes become arrested because of the layering of the shallow crust, which has major effects also on dike-induced stress fields (Gudmundsson, 2003; Bazargan and Gudmundsson, 2019). Gudmundsson and Brenner (2001) and Drymoni et al. (2023) observed stress rotations at contacts with stiffness contrasts, particularly between stiff lava flows and soft layers (breccia, scoria). Before that, laboratory experiments had shown that soft layers may often be effective in arresting hydrofractures (Charlez, 1997; Yew and Weng, 1997). In our models, a simple variation in the stiffness of layers is not enough to generate a stress barrier that could have arrested the second dike (e.g., Figs. 12-13). The stiffness contrast, however, strongly affects stress concentrations at the dike tip and at the surface. Specifically, stresses concentrate in the stiffer layers (layers with greater Young's modulus or E values), as already shown e.g. by Tibaldi et al. (2022), and Drymoni et al. (2023). In all the models (Fig. 10-11-12-13), moving the dike tip closer to the soft (tuff) - stiff (lava or consolidated ash) contact, the tensile stress at the tip of the dike decreases and the tensile stress in the upper lava increases. This is in agreement with the results of Inskip et al. (2020), suggesting that this particular layering (stiff lava above and soft tuff below) favours dike arrest at the contact.

The presence of an extensional stress field (1 MPa) produces a higher concentration of stresses in the stiff layers but does not yield 90° rotation of the principal stresses. However, when horizontal compressive stress is added as a boundary load (Fig. 15), tensile stress concentrations at the tip of the dike decrease so as to encourage dike arrest. Furthermore, we observed that the orientation of the principal stresses rotates, reaching an angle of 90° (with horizontal σ_1 and vertical σ_3) when the horizontal compression is greater than dike overpressure (Fig. 15). The rotation of the principal stresses could cause the deflection of the dike if the tensile stress at the tip was high enough for the dike to continue its propagation or favour its arrest in case of low tensile stress at the tip. The presence of a horizontal compression can therefore contribute to dike arrest, as already demonstrated by Menand et al. (2010) through analogue models, and by Gudmundsson (2003) and Drymoni et al. (2020) through numerical models. In general, the presence of lateral horizontal compression in an area characterised by extensional tectonics can be explained by normal faulting, or by the overpressure of earlier dikes, both of which can temporarily locally change the regional horizontal σ_3 to either σ_2 or σ_1 (Gudmundsson, 2003, 2020). In the Stampar area, normal faults or grabens are absent. Thus, the most likely source of a local horizontal compression is the previous intrusion of the feeder dike (Gudmundsson, 2017), which resulted in the arrest of the later dike (Fig. 14). With regard to the distance between the two dikes, it is known from previous analytical models that Mode I cracks under internal fluid overpressure, such as dikes, provide a zone of compressive stress up to a distance that is similar to about half the length (half the strike dimension) of the crack (Gudmundsson, 2011a). A zone of compressive stresses around a dike-fed volcanic fissure was observed by Andrew and Gudmundsson (2008) through numerical models. This result is also in agreement with Ruz et al. (2020), who observed that previous intrusions can induce a local reorientation of stresses that can, in turn, affect the path of later dikes. In the Stampar case, considering the thickness of the feeder dike, length can be derived from typical length/thickness ratios that are found in the literature for dikes in Iceland (from 300 to 1500; Gudmundsson, 2020). According to these values, we can assume with certainty that, at a distance of 30 m, the host rock was subject to compressive stresses induced by the previous feeder dike. With larger dikes, the distances of induced compressive stresses can be greater, as observed during other diking events in Iceland, such as in Krafla (1975–1984) and in Bardarbunga (2014). In those cases, larger dikes generated temporary “excess spreading rates” out to tens of kilometres, as explained by the numerical models by Andrew and Gudmundsson (2008).

Furthermore, when the feeder dike propagated to the surface, dike-induced compressive stress concentrated in the lava layer (and consolidated ash layer) due to its great stiffness. Considering the overpressure as the difference between the total magmatic pressure in the dike and the minimum principal compressive (maximum tensile) stress σ_3 acting on the dike walls (Kusumoto et al., 2013), if the compressive stress increases, the overpressure of the dike diminishes on approaching the contact between the tuff and the lava layers. Thus, the mechanical contrast between such layers plays a role in the arrest of the non-feeder dike.

Normal faults and grabens have formed or been reactivated during some recent diking episodes in Iceland, such as the 1975–1984 Krafla Fires (Sigurdsson, 1980; Rubin, 1992) and the 2014 Bardarbunga episode (Sigmundsson et al., 2015; Hjartardóttir et al., 2016; Ruch et al., 2016). However, our field observations reveal the lack of any kind of brittle deformation at the surface, even if the tip of the arrested dike is at a very shallow depth (Fig. 6B). Al Shehri and Gudmundsson (2018) and Bazargan and Gudmundsson (2019) investigated the role of layering in inhibiting dike-induced deformation, showing with numerical models how soft layers can make dike-induced surface fracturing difficult, unless the dike is very shallow, has a great overpressure, or both. In our models, when we modify the stiffness of the lava layers, we observe that stresses at the surface increase with increasing stiffness of the lava layer. Nevertheless, if an extensional stress field is applied, tensile and von Mises stress magnitudes at the surface are always high enough to generate fracturing and faulting. Our results differ somewhat from those of Bazargan and Gudmundsson (2019), probably because we are dealing with very shallow depths (5 m) of the tip of the arrested Stampar dike, whereas in their models the arrested dike tip is at a depth of 500 m. However, in our models we observed that layering (with a stiff lava above and a soft tuff below) and the presence of a horizontal compression can reduce the tensile stress concentration at the tip of the dike. Considering that stress concentrations at the tip are generally much higher than stresses at the surface, as observed by Gudmundsson (2003), if the tip stresses are low, they are still lower at the surface and thus cannot generate tension fractures or normal faults at the surface. Therefore, we conclude that the layering, together with the compression caused by the previous intrusion of the feeder dike, can explain not only the arrest of the non-feeder dike, but also the absence of brittle fractures

at the surface.

6. Conclusions

Through a multidisciplinary analysis, we studied the crater row and two dikes associated with the Younger Stampar eruption, in the Reykjanes Peninsula, RP (SW Iceland). One dike (inferred to have been emplaced earlier) is a feeder dike, the other is arrested with its tip at only 5 m below the surface. Our structural data show that the strike of the Younger Stampar crater row/volcanic fissure is consistent with the general NNE-NE strike of eruptive fissures of historical and prehistoric eruptions on the RP. Furthermore, strikes of the dikes cropping out along the sea cliffs studied here are consistent with the orientation of the Younger Stampar crater row. However, there is no dike-induced faulting or tension-fracture formation associated with either of the dikes. Based on bulk rocks and mineral analyses, the two dikes show some differences in their rock and mineral chemistry and modal composition. Our numerical models suggest the following conclusions as regards dike arrest and the lack of dike-induced brittle deformation:

i) Decreasing magmatic overpressures as the non-feeder approached the surface resulted in a decrease in tensile stress concentration at the dike tip, leading to its arrest.

ii) Layering, and specifically the presence of a stiffer lava layer above a softer tuff layer (as observed here), also decreased the tensile stress at the non-feeder dike tip and transferred the stress to the upper (stiff) lava layer. However, the variation of the mechanical properties (stiffness) of the layers is here not enough to generate a classic stress barrier for dikes (with horizontal σ_1).

iii) In a model where the non-feeder dike is subject to horizontal compression due to the previous intrusion of the nearby and earlier feeder dike, tensile concentration of stress at the non-feeder tip becomes reduced. Furthermore, the compressive stress induced by the feeder dike concentrates in stiff lava (and consolidated ash) layers, encouraging the arrest of the non-feeder dike at contact between a soft (below) and a stiff (above) layer.

iv) When the horizontal compressive stress induced by the feeder dike is greater than non-feeder dike overpressure, 90° rotation of the principal stresses occurs ahead of the dike tip, so that σ_1 becomes horizontal forming a classic stress barrier.

v) When tensile and shear stresses at the dike tip decrease, they can become too low to generate brittle deformation at the surface, even if the dike tip is at a very shallow depth, as observed here. We conclude that layering and the presence of a horizontal compression together explain the absence of brittle deformation associated with the arrested dike.

The results presented here can be applied to the whole RP, as well as to other volcanic areas worldwide, characterised by diking episodes.

CRediT authorship contribution statement

Noemi Corti: Conceptualization, Investigation, Writing – original draft, Visualization. **Fabio L. Bonali:** Conceptualization, Investigation, Writing – original draft. **Elena Russo:** Investigation, Writing – original draft. **Kyriaki Drymoni:** Investigation, Writing – review & editing. **Federico Pasquaré Mariotto:** Investigation, Writing – review & editing. **Agust Gudmundsson:** Investigation, Writing – review & editing. **Rosario Esposito:** Investigation, Writing – original draft. **Alessandro Cavallo:** Investigation, Writing – review & editing. **Alessandro Tibaldi:** Writing – review & editing, Supervision.

Declaration of Competing Interest

The authors declare the following financial interests/personal relationships which may be considered as potential competing interests: Alessandro Tibaldi reports financial support was provided by International Lithosphere Program (ILP).

Data availability

Data will be made available on request.

Acknowledgements

We thank the editor Diana Roman and the reviewers John Browning and Abdelsalam Elshaafi for comments which helped improve this manuscript. This work has been carried out under the aegis of Task Force II of the International Lithosphere Program (Leader A. Tibaldi). This manuscript is also an outcome of the Virtual Reality lab for Earth Sciences - GeoVires (https://geovires.unimib.it/), University of Milano-Bicocca. Agisoft Metashape is acknowledged for photogrammetry processing. The work was also supported by funding by the Doctoral school of the University of Milan-Bicocca.

Appendix A. Supplementary data

Supplementary data to this article can be found online at https://doi.org/10.1016/j.jvolgeores.2023.107914.

References

Acocella, V., 2021. Volcano-tectonic processes. Springer Nature.
Acocella, V., Trippanera, D., 2016. How diking affects the tectonomagmatic evolution of slow spreading plate boundaries: Overview and model. Geosphere 12 (3), 867–883.
Ágústsdóttir, T., Woods, J., Greenfield, T., Green, R.G., White, R.S., Winder, T., Brandsdóttir, B., Steinthórsson, S., Soosalu, H., 2016. Strike-slip faulting during the 2014 Bárðarbunga-Holuhraun dike intrusion, Central Iceland. Geophys. Res. Lett. 43 (4), 1495–1503.
Al Shehri, A., Gudmundsson, A., 2018. Modelling of surface stresses and fracturing during dyke emplacement: Application to the 2009 episode at Harrat Lunayyir, Saudi Arabia. J. Volcanol. Geotherm. Res. 356, 278–303.
Amadei, B., Stephansson, O., 1997. Rock Stress and its Measurement (Springer Science & Business Media).
Anderson, A.T., Davis, A.M., Lu, F., 2000. Evolution of Bishop Tuff rhyolitic magma based on melt and magnetite inclusions and zoned phenocrysts. J. Petrol. 41 (3), 449–473.
Andrew, R.E., Gudmundsson, A., 2008. Volcanoes as elastic inclusions: their effects on the propagation of dykes, volcanic fissures, and volcanic zones in Iceland. J. Volcanol. Geotherm. Res. 177 (4), 1045–1054.
Barnett, Z.A., Gudmundsson, A., 2014. Numerical modelling of dykes deflected into sills to form a magma chamber. J. Volcanol. Geotherm. Res. 281, 1–11.
Barsotti, S., Parks, M.M., Pfeffer, M.A., Óladóttir, B.A., Barnie, T., Titos, M.M., Jónsdóttir, K., Pedersen, G.B.M., Hjartardóttir, Á.R., Stefansdóttir, G., Johannsson, T., Arason, Þ., Gudmundsson, M.T., Oddsson, B., Þrastarson, R.H., Ófeigsson, B.G., Vogfjörd, K., Geirsson, H., Hjörvar, T., von Löwis, S., Petersen, G.N., Sigurðsson, E.M., 2023. The eruption in Fagradalsfjall (2021, Iceland): how the operational monitoring and the volcanic hazard assessment contributed to its safe access. Nat. Hazards 116 (3), 3063–3092.
Bazargan, M., Gudmundsson, A., 2019. Dike-induced stresses and displacements in layered volcanic zones. J. Volcanol. Geotherm. Res. 384, 189–205.
Bazargan, M., Gudmundsson, A., 2020. Stresses and displacements in layered rocks induced by inclined (cone) sheets. J. Volcanol. Geotherm. Res. 401, 106965.
Biggs, J., Amelung, F., Gourmelen, N., Dixon, T.H., Kim, S.W., 2009. InSAR observations of 2007 Tanzania rifting episode reveal mixed fault and dyke extension in an immature continental rift. Geophys. J. Int. 179 (1), 549–558.
Bindeman, I.N., Deegan, F.M., Troll, V.R., Thordarson, T., Höskuldsson, Á., Moreland, W. M., Zorn, E.U., Shevchenko, A.V., Walter, T.R., 2022. Diverse mantle components with invariant oxygen isotopes in the 2021 Fagradalsfjall eruption, Iceland. Nat. Commun. 13 (1), 3737.
Bonaccorso, A., Bonforte, A., Calvari, S., Del Negro, C., Di Grazia, G., Ganci, G., Neri, M., Vicari, A., Boschi, E., 2011. The initial phases of the 2008–2009 Mount Etna eruption: a multidisciplinary approach for hazard assessment. J. Geophys. Res. Solid Earth 116 (B3).
Bonali, F.L., Tibaldi, A., Marchese, F., Fallati, L., Russo, E., Corselli, C., Savini, A., 2019. UAV-based surveying in volcano-tectonics: an example from the Iceland rift. J. Struct. Geol. 121, 46–64.
Bonali, F.L., Antoniou, V., Vlasopoulos, O., Tibaldi, A., Nomikou, P., 2020. Selfie Drones for 3D Modelling, Geological Mapping and Data Collection: Key Examples from Santorini Volcanic Complex, Greece. In GISTAM, pp. 119–128.
Borromeo, L., Andò, S., Bersani, D., Garzanti, E., Gentile, P., Mantovani, L., Tribaudino, M., 2022. Detrital orthopyroxene as a tracer of geodynamic setting: a Raman and SEM-EDS provenance study. Chem. Geol. 596, 120809.
Browning, J., Karaoğlu, Ö.Z.G.Ü.R., Bayer, Ö., Turgay, M.B., Acocella, V., 2021. Stress fields around magma chambers influenced by elastic thermo-mechanical deformation: implications for forecasting chamber failure. Bull. Volcanol. 83, 1–13.

Burns, J.H.R., Delparte, D., 2017. Comparison of commercial structure-from-motion photogrammetry software used for underwater three-dimensional modeling of coral reef environments. Int. Arch. Photogramm. Remote Sens. Spat. Inform. Sci. 42, 127.
Calais, E., d'Oreye, N., Albaric, J., Deschamps, A., Delvaux, D., Déverchère, J., Ebinger, C., Ferdinand, R.W., Kervyn, F., Macheyeki, A.S., Oyen, A., Perrot, J., Saria, E., Smets, B., Stamps, D.S., Wauthier, C., 2008. Strain accommodation by slow slip and dyking in a youthful continental rift, East Africa. Nature 456 (7223), 783–787.
Chadwick Jr., W.W., Embley, R.W., 1998. Graben formation associated with recent dike intrusions and volcanic eruptions on the mid-ocean ridge. J. Geophys. Res. Solid Earth 103 (B5), 9807–9825.
Charlez, P.A., 1997. Rock Mechanics, Vol. 2. Petroleum Applications.
Clifton, A.E., Kattenhorn, S.A., 2006. Structural architecture of a highly oblique divergent plate boundary segment. Tectonophysics 419 (1–4), 27–40.
Clifton, A.E., Schlische, R.W., 2003. Fracture populations on the Reykjanes Peninsula, Iceland: comparison with experimental clay models of oblique rifting. J. Geophys. Res. Solid Earth 108 (B2).
Clunes, M., Browning, J., Marquardt, C., Cortez, J., Drymoni, K., Kavanagh, J., 2023. Inclination and heterogeneity of layered geological sequences influence dike-induced ground deformation. Geology 51 (3), 278–283.
Corti, N., Bonali, F.L., Pasquaré Mariotto, F., Tibaldi, A., Russo, E., Rigoni, V., Bressan, S., 2021. Fracture Kinematics and Holocene stress Field at the Krafla Rift, Northern Iceland. Geosciences 11 (2), 101.
Danyushevsky, L.V., Plechov, P., 2011. Petrolog3: Integrated software for meter crystallization processes. Geochem. Geophys. Geosyst. 12 (7).
Delaney, P.T., Pollard, D.D., Ziony, J.I., McKee, E.H., 1986. Field relations between dikes and joints: Emplacement processes and paleostress analysis. J. Geophys. Res. Solid Earth 91 (B5), 4920–4938.
DeMets, C., Gordon, R.G., Argus, D.F., 2010. Geologically current plate motions. Geophys. J. Int. 181 (1), 1–80.
Drymoni, K., Browning, J., Gudmundsson, A., 2020. Dyke-arrest scenarios in extensional regimes: Insights from field observations and numerical models, Santorini, Greece. J. Volcanol. Geotherm. Res. 396, 106854.
Drymoni, K., Russo, E., Tibaldi, A., Corti, N., Bonali, F.L., Pasquaré Mariotto, F., 2023. Dyke-induced graben formation in a heterogeneous succession on Mt. Etna: Insights from field observations and FEM numerical models. J. Volcanol. Geotherm. Res. 107712.
Ebinger, C.J., Keir, D., Ayele, A., Calais, E., Wright, T.J., Belachew, M., Hammond, J.O.S., Campbell, E., Buck, W.R., 2008. Capturing magma intrusion and faulting processes during continental rupture: seismicity of the Dabbahu (Afar) rift. Geophys. J. Int. 174 (3), 1138–1152.
Einarsson, P., 2008. Plate boundaries, rifts and transforms in Iceland. Jökull 58 (12), 35–58.
Einarsson, P., Sæmundsson, K., 1987. Earthquake epicenters 1982–1985 and volcanic systems in Iceland. In: Sigfússon, Þ.I. (Ed.), Í hlutarins eðli, Festschrift for Þorbjörn Sigurgeirsson. Menningarsjóður, Reykjavík (map).
Esposito, R., 2021. In: Lecumberri-Sanchez, P., Steele-MacInnis, M., Kontak, D.J. (Eds.), A protocol and review of methods to select, analyze and interpret melt inclusions to determine pre-eruptive volatile contents of magmas. Fluid and Melt Inclusions: Applications to Geologic Processes, 49. Mineralogical Association of Canada Short Course, pp. 163–194.
Esposito, R., Badescu, K., Steele-MacInnis, M., Cannatelli, C., De Vivo, B., Lima, A., Bodnar, R.J., Manning, C.E., 2018. Magmatic evolution of the Campi Flegrei and Procida volcanic fields, Italy, based on interpretation of data from well-constrained melt inclusions. Earth Sci. Rev. 185, 325–356.
Flóvenz, Ó.G., Wang, R., Hersir, G.P., Dahm, T., Hainzl, S., Vassileva, M., Drouin, V., Heimann, S., Isken, M.P., Gudnason, E.Á., Ágústsson, K., Ágústsdóttir, T., Horálek, J., Motagh, M., Walter, T.R., Rivalta, E., Jousset, P., Krawczyk, C.M., Milkereit, C., 2022. Cyclical geothermal unrest as a precursor to Iceland's 2021 Fagradalsfjall eruption. Nat. Geosci. 15 (5), 397–404.
Forslund, T., Gudmundsson, A., 1991. Crustal spreading due to dikes and faults in southwest Iceland. J. Struct. Geol. 13 (4), 443–457.
Forslund, T., Gudmundsson, A., 1992. Structure of Tertiary and Pleistocene normal faults in Iceland. Tectonics 11 (1), 57–68.
Fowler, A.P., Zierenberg, R.A., 2016a. Elemental changes and alteration recorded by basaltic drill core samples recovered from in situ temperatures up to 345° C in the active, seawater-recharged Reykjanes geothermal system, Iceland. Geochem. Geophys. Geosyst. 17 (11), 4772–4801.
Fowler, A.P., Zierenberg, R.A., 2016b. Geochemical bias in drill cutting samples versus drill core samples returned from the Reykjanes Geothermal System, Iceland. Geothermics 62, 48–60.
Gee, M.A.M., Thirlwall, M.F., Taylor, R.N., Lowry, D., Murton, B.J., 1998. Crustal processes: major controls on Reykjanes Peninsula lava chemistry, SW Iceland. J. Petrol. 39 (5), 819–839.
Geshi, N., Kusumoto, S., Gudmundsson, A., 2012. Effects of mechanical layering of host rocks on dike growth and arrest. J. Volcanol. Geotherm. Res. 223, 74–82.
Geyer, A., Gottsmann, J., 2010. The influence of mechanical stiffness on caldera deformation and implications for the 1971–1984 Rabaul uplift (Papua New Guinea). Tectonophysics 483 (3–4), 399–412.
Grandin, R., Socquet, A., Binet, R., Klinger, Y., Jacques, E., De Chabalier, J.B., King, G.C. P., Lasserre, C., Tait, S., Tapponnier, P., Delorme, A., Pinzuti, P., 2009. September 2005 Manda Hararo-Dabbahu rifting event, Afar (Ethiopia): constraints provided by geodetic data. J. Geophys. Res. Solid Earth 114 (B8).
Gretener, P.E., 1969. On the mechanics of the intrusion of sills. Can. J. Earth Sci. 6 (6), 1415–1419.
Gudmundsson, A., 1986a. Formation of crustal magma chambers in Iceland. Geology 14 (2), 164–166.
Gudmundsson, A., 1986b. Mechanical aspects of postglacial volcanism and tectonics of the Reykjanes Peninsula, Southwest Iceland. J. Geophys. Res. Solid Earth 91 (B12), 12711–12721.
Gudmundsson, A., 1987. Geometry, formation and development of tectonic fractures on the Reykjanes Peninsula, Southwest Iceland. Tectonophysics 139 (3–4), 295–308.
Gudmundsson, A., 2003. Surface stresses associated with arrested dykes in rift zones. Bull. Volcanol. 65 (8), 606–619.
Gudmundsson, A., 2011a. Rock Fractures in Geological Processes. Cambridge University Press.
Gudmundsson, A., 2011b. Deflection of dykes into sills at discontinuities and magma-chamber formation. Tectonophysics 500 (1–4), 50–64.
Gudmundsson, A., 2017. The Glorious Geology of Iceland's Golden Circle (p. 334). Springer International Publishing, Cham, Switzerland.
Gudmundsson, A., 2020. Volcanotectonics: Understanding the Structure, Deformation and Dynamics of Volcanoes. Cambridge University Press.
Gudmundsson, A., 2022. The propagation paths of fluid-driven fractures in layered and faulted rocks. Geol. Mag. 159 (11−12), 1978–2001.
Gudmundsson, A., Brenner, S.L., 2001. How hydrofractures become arrested. Terra Nova 13 (6), 456–462.
Gudmundsson, A., Marinoni, L.B., Marti, J., 1999. Injection and arrest of dykes: implications for volcanic hazards. J. Volcanol. Geotherm. Res. 88 (1–2), 1–13.
Gurenko, A.A., Sobolev, A.V., Kononkova, N.N., 1990. Petrology of primary melt of riftogenic tholeiites from Reikjanes Peninsula, Iceland. Geokhimiya 8, 1137–1150.
Haimson, B.C., Rummel, F., 1982. Hydrofracturing stress measurements in the Iceland research drilling project drill hole at Reydarfjordur, Iceland. J. Geophys. Res. Solid Earth 87 (B8), 6631–6649.
Halldórsson, S.A., Marshall, E.W., Caracciolo, A., Matthews, S., Bali, E., Rasmussen, M.B., Ranta, E., Gunnarsson Robin, J., Guðfinnsson, G.H., Sigmarsson, O., Maclennan, J., Jackson, M.G., Whitehouse, M.J., Jeon, H., van der Meer, Q.H.A., Mibei, G.K., Kalliokoski, M.H., Repczynska, M.M., Rúnarsdóttir, R.H., Sigurðsson, G., Pfeffer, M. A., Scott, S.W., Kjartansdóttir, R., Kleine, B.I., Oppenheimer, C., Aiuppa, A., Ilyinskaya, E., Bitetto, M., Giudice, G., Stefánsson, A., 2022. Rapid shifting of a deep magmatic source at Fagradalsfjall volcano, Iceland. Nature 609 (7927), 529–534.
Heimisson, E.R., Segall, P., 2020. Physically consistent modeling of dike-Induced deformation and seismicity: Application to the 2014 Bárðarbunga dike, Iceland. J. Geophys. Res. Solid Earth 125 (2) e2019JB018141.
Hjartardóttir, Á.R., Einarsson, P., Gudmundsson, M.T., Högnadóttir, T., 2016. Fracture movements and graben subsidence during the 2014 Bárðarbunga dike intrusion in Iceland. J. Volcanol. Geotherm. Res. 310, 242–252.
Inskip, N.D.F., Browning, J., Meredith, P.G., Gudmundsson, A., 2020. Conditions for fracture arrest in layered rock sequences. Results Geophys. Sci. 1, 100001.
Isida, M., 1955. On the tension of a strip with a central elliptic hole (Pasrt 1). Trans. Japan Soc. Mech. Eng. 21 (107), 507.
Jakobsson, S.P., Jónsson, J., Shido, F., 1978. Petrology of the western Reykjanes peninsula, Iceland. J. Petrol. 19 (4), 669–705.
James, M.R., Robson, S., 2012. Straightforward reconstruction of 3D surfaces and topography with a camera: Accuracy and geoscience application. J. Geophys. Res. Earth 117 (F3).
James, M.R., Robson, S., Smith, M.W., 2017. 3-D uncertainty-based topographic change detection with structure-from-motion photogrammetry: precision maps for ground control and directly georeferenced surveys. Earth Surf. Process. Landf. 42 (12), 1769–1788.
Kavanagh, J.L., Menand, T., Sparks, R.S.J., 2006. An experimental investigation of sill formation and propagation in layered elastic media. Earth Planet. Sci. Lett. 245 (3–4), 799–813.
Kokfelt, T.F., Hoernle, K.A.J., Hauff, F., Fiebig, J., Werner, R., Garbe-Schoenberg, D., 2006. Combined trace element and Pb-Nd–Sr-O isotope evidence for recycled oceanic crust (upper and lower) in the Iceland mantle plume. J. Petrol. 47 (9), 1705–1749.
Koornneef, J.M., Stracke, A., Bourdon, B., Meier, M.A., Jochum, K.P., Stoll, B., Grönvold, K., 2012. Melting of a two-component source beneath Iceland. J. Petrol. 53 (1), 127–157.
Kusumoto, S., Geshi, N., Gudmundsson, A., 2013. Aspect ratios and magma overpressures of non-feeder dikes observed in the Miyake-jima volcano (Japan), and fracture toughness of its upper part. Geophys. Res. Lett. 40 (6), 1065–1068.
Le Maitre, R.W., Streckeisen, A., Zanettin, B., Le Bas, M.J., Bonin, B., Bateman, P., Bellieni, G., Dudek, A., Efremova, S., Keller, J., Lameyre, J., Sabine, P.A., Schmid, R., Sørensen, H., Woolley, A.R., 2002. Igneous rocks. A Classification and Glossary of Terms: Recommendations of the International Union of Geological Sciences Subcommission on the Systematics of Igneous Rocks. Cambridge University Press, Cambridge, p. 2.
Maccaferri, F., Bonafede, M., Rivalta, E., 2010. A numerical model of dyke propagation in layered elastic media. Geophys. J. Int. 180 (3), 1107–1123.
Maccaferri, F., Bonafede, M., Rivalta, E., 2011. A quantitative study of the mechanisms governing dike propagation, dike arrest and sill formation. J. Volcanol. Geotherm. Res. 208 (1–2), 39–50.
Maccaferri, F., Rivalta, E., Passarelli, L., Aoki, Y., 2016. On the mechanisms governing dike arrest: insight from the 2000 Miyakejima dike injection. Earth Planet. Sci. Lett. 434, 64–74.
Magee, C., Jackson, C.A.L., 2021. Can we relate the surface expression of dike-induced normal faults to subsurface dike geometry? Geology 49 (4), 366–371.
Mastin, L.G., Pollard, D.D., 1988. Surface deformation and shallow dike intrusion processes at Inyo Craters, Long Valley, California. J. Geophys. Res. Solid Earth 93 (B11), 13221–13235.

Menand, T., 2008. The mechanics and dynamics of sills in layered elastic rocks and their implications for the growth of laccoliths and other igneous complexes. Earth Planet. Sci. Lett. 267 (1–2), 93–99.
Menand, T., Daniels, K.A., Benghiat, P., 2010. Dyke propagation and sill formation in a compressive tectonic environment. J. Geophys. Res. Solid Earth 115 (B8).
Micheletti, N., Chandler, J.H., Lane, S.N., 2015. Investigating the geomorphological potential of freely available and accessible structure-from-motion photogrammetry using a smartphone. Earth Surf. Process. Landf. 40 (4), 473–486.
Morimoto, N., 1988. Nomenclature of Pyroxenes. Mineral. Petrol. 39, 55–76.
Murray, J.B., Pullen, A.D., 1984. Three-dimensional model of the feeder conduit of the 1983 eruption of Mt. Etna volcano, from ground deformation measurements. Bull. Volcanol. 47 (4), 1145–1163.
Nobile, A., Pagli, C., Keir, D., Wright, T.J., Ayele, A., Ruch, J., Acocella, V., 2012. Dike-fault interaction during the 2004 Dallol intrusion at the northern edge of the Erta Ale Ridge (Afar, Ethiopia). Geophys. Res. Lett. 39 (19).
Pallister, J.S., McCausland, W.A., Jónsson, S., Lu, Z., Zahran, H.M., Hadidy, S.E., Aburukbah, A., Stewart, I.C.F., Lundgren, P.R., White, R.A., Moufti, M.R.H., 2010. Broad accommodation of rift-related extension recorded by dyke intrusion in Saudi Arabia. Nat. Geosci. 3 (10), 705–712.
Parsons, T., Sleep, N.H., Thompson, G.A., 1992. Host rock rheology controls on the emplacement of tabular intrusions: implications for underplating of extending crust. Tectonics 11 (6), 1348–1356.
Pasquaré Mariotto, F., Antoniou, V., Drymoni, K., Bonali, F.L., Nomikou, P., Fallati, L., Karatzaferis, O., Vlasopoulos, O., 2021. Virtual geosite communication through a Webgis platform: a case study from Santorini island (Greece). Appl. Sci. 11 (12), 5466.
Peate, D.W., Baker, J.A., Jakobsson, S.P., Waight, T.E., Kent, A.J., Grassineau, N.V., Skovgaard, A.C., 2009. Historic magmatism on the Reykjanes Peninsula, Iceland: a snap-shot of melt generation at a ridge segment. Contrib. Mineral. Petrol. 157 (3), 359–382.
Philipp, S.L., Afşar, F., Gudmundsson, A., 2013. Effects of mechanical layering on hydrofracture emplacement and fluid transport in reservoirs. Front. Earth Sci. 1, 4.
Pollard, D.D., Delaney, P.T., Duffield, W.A., Endo, E.T., Okamura, A.T., 1983. Surface deformation in volcanic rift zones. In: Developments in Geotectonics, Vol. 19. Elsevier, pp. 541–584.
Putirka, K.D., 2017. Down the crater: where magmas are stored and why they erupt. Elements 13 (1), 11–16.
Rivalta, E., Böttinger, M., Dahm, T., 2005. Buoyancy-driven fracture ascent: experiments in layered gelatine. J. Volcanol. Geotherm. Res. 144 (1–4), 273–285.
Rivalta, E., Taisne, B., Bunger, A.P., Katz, R.F., 2015. A review of mechanical models of dike propagation: Schools of thought, results and future directions. Tectonophysics 638, 1–42.
Roman, D.C., Cashman, K.V., 2006. The origin of volcano-tectonic earthquake swarms. Geology 34 (6), 457–460.
Rubin, A.M., 1992. Dike-induced faulting and graben subsidence in volcanic rift zones. J. Geophys. Res. Solid Earth 97 (B2), 1839–1858.
Rubin, A.M., Gillard, D., 1998. Dike-induced earthquakes: Theoretical considerations. J. Geophys. Res. Solid Earth 103 (B5), 10017–10030.
Rubin, A.M., Pollard, D.D., 1988. Dike-induced faulting in rift zones of Iceland and Afar. Geology 16 (5), 413–417.
Ruch, J., Wang, T., Xu, W., Hensch, M., Jónsson, S., 2016. Oblique rift opening revealed by reoccurring magma injection in Central Iceland. Nat. Commun. 7 (1), 1–7.
Ruz, J., Browning, J., Cembrano, J., Iturrieta, P., Gerbault, M., Sielfeld, G., 2020. Field observations and numerical models of a Pleistocene-Holocene feeder dyke swarm associated with a fissure complex to the east of the Tatara-San Pedro-Pellado complex, Southern Volcanic Zone, Chile. J. Volcanol. Geotherm. Res. 404, 107033.
Saemundsson, K., Sigurgeirsson, M.Á., Hjartarson, A., Kaldal, I., Kristinsson, S.G., 2016. Geological Map of Southwest Iceland, 1:100 000, 2nd ed. Iceland GeoSurvey.
Saemundsson, K., Sigurgeirsson, M.Á., Friðleifsson, G.Ó., 2020. Geology and structure of the Reykjanes volcanic system, Iceland. J. Volcanol. Geotherm. Res. 391, 106501.
Schultz, R., 1995. Limits on strength and deformation properties of jointed basaltic rock masses. Rock Mech. Rock. Eng. 28 (1), 1–15.
Segall, P., 2013. Volcano deformation and eruption forecasting. Geol. Soc. Lond. Spec. Publ. 380 (1), 85–106.
Sigmundsson, F., Hooper, A., Hreinsdóttir, S., Vogfjörd, K.S., Ófeigsson, B.G., Heimisson, E.R., Dumont, S., Parks, M., Spaans, K., Gudmundsson, G.B., Drouin, V., Árnadóttir, T., Jónsdóttir, K., Gudmundsson, M.T., Högnadóttir, T., Fridriksdóttir, H. M., Hensch, M., Einarsson, P., Magnússon, E., Samsonov, S., Brandsdóttir, B., White, R.S., Ágústsdóttir, T., Greenfield, T., Green, R.G., Hjartardóttir, Á.R., Pedersen, R., Bennett, R.A., Geirsson, H., La Femina, P.C., Björnsson, H., Pálsson, F., Sturkell, E., Bean, C.J., Möllhoff, M., Braiden, A.K., Eibl, E.P.S., 2015. Segmented lateral dyke growth in a rifting event at Bárðarbunga volcanic system, Iceland. Nature 517 (7533), 191–195.
Sigmundsson, F., Parks, M., Hooper, A., Geirsson, H., Vogfjörd, K.S., Drouin, V., Ófeigsson, B.G., Hreinsdóttir, S., Hjaltadóttir, S., Jónsdóttir, K., Einarsson, P., Barsotti, S., Horálek, J., Ágústsdóttir, T., 2022. Deformation and seismicity decline before the 2021 Fagradalsfjall eruption. Nature 609 (7927), 523–528.
Sigurdsson, O., 1980. Surface deformation of the Krafla fissure swarm in two rifting events. J. Geophys. 47 (1), 154–159.
Sigurgeirsson, M.Á., 1992. Tephra Formation at Reykjanes (Gjóskumyndanir á Reykjanesi, in Icelandic) (Doctoral Dissertation, MS-thesis, University of Iceland).
Sigurgeirsson, M.Á., 1995. M. Á. YNGRA-STAMPAGOSID IN REYKJANES (in Icelandic). Náttúrufræðingurinn 64 (3) bls. 211-230.
Sinton, J., Grönvold, K., Sæmundsson, K., 2005. Postglacial eruptive history of the western volcanic zone, Iceland. Geochem. Geophys. Geosyst. 6 (12).
Spera, F.J., 2000. Physical Properties of Magma. Encyclopedia on Volcanoes.
Stein, R.S., Briole, P., Ruegg, J.C., Tapponnier, P., Gasse, F., 1991. Contemporary, Holocene, and Quaternary deformation of the Asal Rift, Djibouti: Implications for the mechanics of slow spreading ridges. J. Geophys. Res. Solid Earth 96 (B13), 21789–21806.
Swanson, D.A., 1976. Displacement of the south flank of Kilauea volcano: the result of forceful intrusion of magma into the rift zones. US Geol. Surv. Prof. Pap. 963, 39.
Thomson, K., 2007. Determining magma flow in sills, dykes and laccoliths and their implications for sill emplacement mechanisms. Bull. Volcanol. 70 (2), 183–201.
Tibaldi, A., 1995. Morphology of pyroclastic cones and tectonics. J. Geophys. Res. Solid Earth 100 (B12), 24521–24535.
Tibaldi, A., Bonali, F.L., 2017. Intra-arc and back-arc volcano-tectonics: Magma pathways at Holocene Alaska-Aleutian volcanoes. Earth Sci. Rev. 167, 1–26.
Tibaldi, A., Pasquarè Mariotto, F., 2008. A new mode of inner volcano growth: the “flower intrusive structure”. Earth Planet. Sci. Lett. 271 (1–4), 202–208.
Tibaldi, A., Bonali, F.L., Pasquaré Mariotto, F., Rust, D., Cavallo, A., D’urso, A., 2013. Structure of regional dykes and local cone sheets in the Midhyrna-Lysuskard area, Snaefellsnes Peninsula (NW Iceland). Bull. Volcanol. 75 (11), 1–16.
Tibaldi, A., Bonali, F.L., Corti, N., Russo, E., Drymoni, K., De Beni, E., Branca, S., Neri, M., Cantarero, M., Pasquaré Mariotto, F., 2022. Surface deformation during the 1928 fissure eruption of Mt. Etna (Italy): nsights from field data and FEM numerical modelling. Tectonophysics 837, 229468.
Townsend, M.R., Pollard, D.D., Smith, R.P., 2017. Mechanical models for dikes: a third school of thought. Tectonophysics 703, 98–118.
Trippanera, D., Ruch, J., Acocella, V., Rivalta, E., 2015. Experiments of dike-induced deformation: insights on the long-term evolution of divergent plate boundaries. J. Geophys. Res. Solid Earth 120 (10), 6913–6942.
Trippanera, D., Ruch, J., Passone, L., Jónsson, S., 2019. Structural mapping of dike-induced faulting in Harrat Lunayyir (Saudi Arabia) by using high resolution drone imagery. Front. Earth Sci. 7, 168.
Urbani, S., Acocella, V., Rivalta, E., Corbi, F., 2017. Propagation and arrest of dikes under topography: Models applied to the 2014 Bardarbunga (Iceland) rifting event. Geophys. Res. Lett. 44 (13), 6692–6701.
Wright, T.J., Ebinger, C., Biggs, J., Ayele, A., Yirgu, G., Keir, D., Stork, A., 2006. Magma-maintained rift segmentation at continental rupture in the 2005 Afar dyking episode. Nature 442 (7100), 291–294.
Xu, W., Jónsson, S., Corbi, F., Rivalta, E., 2016. Graben formation and dike arrest during the 2009 Harrat Lunayyir dike intrusion in Saudi Arabia: Insights from InSAR, stress calculations and analog experiments. J. Geophys. Res. Solid Earth 121 (4), 2837–2851.
Yew, C.H., Weng, X., 1997. Mechanics of Hydraulic Fracturing. Houston, Texas.